IMAGE: A MAP OF THE STARS OF THE ORION CONSTELLATION

Print ISSN: 2631-8490 Online ISSN: 2631-8504

JournalPreview

London Journal of Research in Science: Natural & Formal

Volume 25 | Issue 8 | Compilation 1.0

Great Britain Journals Press

WWW.JOURNALSPRESS.COM

Journal Content
In this Issue

Great Britain Journals Press

A Dynamic Framework for Mass-Energy Interaction: Exploring the Role of Time and Relativity

George Petropoulos

ABSTRACT

While the relationship between mass and energy is well-established, in classical and relativistic frameworks, the dynamic interaction between mass, energy, and time has not been fully explored. This study examines how the introduction of time into mass-energy interaction influences the behavior of mass, proposing a new framework in which mass is considered not a static quantity but a dynamic entity that interacts with energy and time. Furthermore, it explores whether under certain conditions, the efficient utilization of energy could theoretically allow for travel at speeds potentially exceeding that of light. This paper extends the conceptualization of energy by considering mass not as a static entity but as a dynamic quantity. It explores how mass distributes received energy and its behavior under various values of energy and time. The investigation begins with the fundamental form of mass, specifically the point energy mass, which is influenced by both energy and time. The study then expands to encompass larger and more complex forms of mass, analyzing the generalized effects of energy and time on their behavior. Additionally, the study examines the roles of space and speed in relation to energy and time, incorporating in the investigation fundamental equations of relativity, including Lorentz transformation and mass energy equivalence. The findings suggest the possibility of mass traveling at speeds that would be considered as limited until now, by setting appropriate mass factors.

Keywords: NA

Classification: LCC Code: QC793.5.E425

Language: English

Great Britain Journals Press

LJP Copyright ID: 925681
Print ISSN: 2631-8490
Online ISSN: 2631-8504

London Journal of Research in Science: Natural & Formal

Volume 25 | Issue 8 | Compilation 1.0

A Dynamic Framework for Mass-Energy Interaction: Exploring the Role of Time and Relativity

George Petropoulos

ABSTRACT

While the relationship between mass and energy is well-established, in classical and relativistic frameworks, the dynamic interaction between mass, energy, and time has not been fully explored. This study examines how the introduction of time into mass-energy interaction influences the behavior of mass, proposing a new framework in which mass is considered not a static quantity but a dynamic entity that interacts with energy and time. Furthermore, it explores whether under certain conditions, the efficient utilization of energy could theoretically allow for travel at speeds potentially exceeding that of light. This paper extends the conceptualization of energy by considering mass not as a static entity but as a dynamic quantity. It explores how mass distributes received energy and its behavior under various values of energy and time. The investigation begins with the fundamental form of mass, specifically the point energy mass, which is influenced by both energy and time. The study then expands to encompass larger and more complex forms of mass, analyzing the generalized effects of energy and time on their behavior. Additionally, the study examines the roles of space and speed in relation to energy and time, incorporating in the investigation fundamental equations of relativity, including Lorentz transformation and mass energy equivalence. The findings suggest the possibility of mass traveling at speeds that would be considered as limited until now, by setting appropriate mass factors.

Author: Naval Architect & Marine Engineer (NTUA), Integrated Master Energy Production & Management (NTUA), MSc 66 Iros Konstantopoulou Str., Byron 16231, Attika, Greece.

I. INTRODUCTION

This study investigates energy distribution equations and models within mass structures and the behavioral transformations exhibited by mass following energy absorption, which explain the relation of mass with energy and time which is missing from current framework. The research extends beyond prior studies by employing a dynamic approach to analyze mass, tracking its temporal evolution from initial energy configurations to bigger and complex forms of mass. However, previous models are used to investigate relation with the limitations that these models apply, such as the speed limit a mass can travel.

The methodological framework commences with an examination of how point energy mass responds to energy while evolving over time. Traditional energy expressions reveal limitations when mass is held constant, with spatial changes considered solely as time-dependent functions. This framework challenges these traditional conceptualizations by exploring energy distribution to mass, thereby enabling a comprehensive study of resultant mass behaviors.

London Journal of Research in Science: Natural & Formal

This expanded perspective on energy distribution results in differential equations that incorporate energy, time, space, and mass. Solutions to these equations uncover fundamental connections between space and speed and energy and time offering insights into potential mass transit at speeds, possibly, higher than light, initially being considered at theoretical level. Two- and three-dimensional visualizations depict individual variable changes against energy and time durations, illustrating their combined effects.

II. METHODOLOGY

There are two ways to approach the relation between energy and mass. The one is the classical that combines various expressions of energy, including potential energy and kinetic energy, whereas the second approach is the relativistic one.

Starting the investigation with the classical expression, let us consider a mass that is located at a height h from the surface of earth. The potential energy at this height is calculated as:

$$E_p = m \cdot g \cdot h \quad (1)$$

where g is the gravitational field strength and h is the measure of height h.

If the mass is let it moves towards the ground and the potential energy is transformed to kinetic energy. Just before touching the ground the kinetic energy of the mass is calculated as:

$$E_k = \frac{1}{2} m \cdot |\vec{u}|^2 \quad (2)$$

Where $|\vec{u}|$ is the magnitude of the speed $\vec{u}$ of mass just before touching the ground and is calculated as:

$$|\vec{u}| = \sqrt{2 \cdot g \cdot h} \quad (3)$$

At any position n the energy of mass is:

$$E_n = \frac{1}{2} m \cdot |\vec{u}_n|^2 + m \cdot g \cdot h_n \quad (4)$$

As it is widely known, if the gravitational field strength g is dimensionally analysed, it is measured in units $g = \frac{(kg)}{(s^2)}$ (5) . If the term $f_t = \frac{1}{(s^2)}$ (6) is considered as second derivative, then the gravity constant would imply the second derivative of mass. This makes one wonder if there could be another way to express mass so that the term f_t has a logical meaning.

The energy of a mass is measured in Joule (J), the dimensional analysis of which is: $J = (kg) \cdot (m^2) \cdot \frac{1}{(s^2)}$ [1], [2], [3], [4] (7). In this case it can be considered that the energy a mass holds is expressed by the contribution of the space squared, the mass, and the reverse time squared. The existence of reverse time can be considered a differentiation of a quantity over time.

2.1. analysis of the model

In general, when studying energy, it is considered that the differentiation over time applies only to space. However, it has been proven [5] that mass is also time-dependent, and the generic expression of point energy mass (pem) in such a case is:

$$m(\varepsilon, \vec{s}, t) = \mu_{0,g} e^{i(\theta(t)+\theta(\varepsilon)-\theta(\vec{s})+\varphi)} \tag{8}$$

so that:

$$\mu_{0,g} = g_\varepsilon g_t g'_{\vec{s}} \tag{9}$$

and

$$g_t = \sqrt{\frac{1}{\omega^4} + (C'_1 t + C'_2)^2 - \frac{2}{\omega^2}(C'_1 t + C'_2)\cos(\omega(t - t_1))}, |g(t)| \geq 0 \tag{10}$$

$$g_\varepsilon = \frac{2}{\alpha}\sin\left(\frac{\alpha}{2}(\varepsilon - \varepsilon_1)\right) \tag{11}$$

$$\text{and } \theta(\varepsilon) = \frac{\alpha}{2}(\varepsilon + \varepsilon_1) \tag{12}$$

$$g'_{\vec{s}} = |g'(\vec{s})| = \frac{1}{\sqrt{{c_k}^2 + (\lambda\vec{k}\cdot\vec{s} + \lambda_v)^2 - 2c_\kappa\lambda(\vec{k}\cdot\vec{s} + c_\lambda)\cos(\vec{k}\cdot(\vec{s} - \vec{s}_0))}} \tag{13}$$

$$\tan\theta(t) = \frac{\sin(\omega t) - \omega^2(C'_1 t + C'_2)\sin(\omega t_1)}{\cos(\omega t) - \omega^2(C'_1 t + C'_2)\cos(\omega t_1)} \tag{14}$$

Also:

$$\theta(\varepsilon) = \frac{\alpha}{2}(\varepsilon + \varepsilon_1) \tag{15}$$

$$\tan\theta(\vec{s}) = \frac{-c_\kappa \sin(\vec{k}\cdot\vec{s}) + \lambda(\vec{k}\cdot\vec{s} + c_\lambda)\sin(\vec{k}\cdot\vec{s}_0)}{-c_\kappa \cos(\vec{k}\cdot\vec{s}) + \lambda(\vec{k}\cdot\vec{s} + c_\lambda)\cos(\vec{k}\cdot\vec{s}_0)} \tag{16}$$

Another expression of mass that derives from the analysis of the factor g_t is:

$$m(\varepsilon, \vec{s}, t) = |\mu_A| e^{i\varphi_{\mu A}} - |\mu_B| e^{i\varphi_{\mu B}} \tag{17}$$

considering:

$$|\mu_A(\varepsilon)| = \mu_{0,\varepsilon} = 2\frac{|\vec{\kappa}|^2}{\alpha\omega^2}\sin\left(\frac{\alpha}{2}(\varepsilon - \varepsilon_1)\right) \geq 0 \tag{18}$$

and

$$\varphi_{\mu_A} = \omega t - \vec{k}\cdot\vec{s} - \frac{\alpha}{2}(\varepsilon_1 + \varepsilon) + \varphi \tag{19}$$

Also:

$$|\mu_B(\varepsilon)| = 2\frac{|\vec{\kappa}|^2}{\alpha\omega^2}\sin\left(\frac{\alpha}{2}(\varepsilon - \varepsilon_1)\right)\omega^2(C_1' t + C_2') \geq 0 \tag{20}$$

and

$$\varphi_{\mu_B} = \omega t_1 - \vec{k}\cdot\vec{s} - \frac{\alpha}{2}(\varepsilon_1 + \varepsilon) + \varphi \tag{21}$$

In other words:

$$m(\varepsilon, \vec{s}, t) = \mu_{0,\varepsilon} e^{i(\omega t - \vec{k}\cdot\vec{s} + \frac{\alpha}{2}(\varepsilon_1+\varepsilon)+\varphi)} - \mu_{0,\varepsilon}\omega^2(C_1' t + C_2')e^{i\left(\omega t_1 - \vec{k}\cdot\vec{s} + \frac{\alpha}{2}(\varepsilon_1+\varepsilon)+\varphi\right)} \tag{22}$$

If the quantities of space and energy contained are considered constants, the mass can be expressed as time-dependent as follows:

$$m(t) = \mu_0 e^{i(\omega t+\theta)} - \omega^2\mu_0(C_1' t + C_2')e^{i(\omega t_1+\theta)} \tag{23}$$

whereas the generic format, as expressed in equation (1), considering only the time as the variable, is:

$$m(t) = \mu_{0,g} e^{i(\theta(t)+\varphi)} \tag{24}$$

Considering the dimensional analysis of Joule (J), the competition of time is expressed as $f_t = \frac{1}{(s^2)}$ (25), which can also be expressed as $f_t = \frac{1}{(s)}\frac{1}{(s)}$ (26). If this approach is combined with the expression of mass developed in relations (8) and (23), the differentiation over time can apply not only to the quantity of space but also to the quantity of mass. Then, starting through the dimensional analysis, the Joule expression can be expressed as follows:

$$J = \frac{(kg)}{(s^2)}\cdot(m^2) + \frac{(kg)}{(s)}\cdot\frac{(m^2)}{(s)} + (kg)\cdot\frac{(m^2)}{(s^2)} \tag{27}$$

which, in terms of the respective quantities, is expressed on one axis as:

$$E = \frac{d^2m}{dt^2} \cdot x^2 + \frac{dm}{dt} \cdot \frac{dx^2}{dt} + m \cdot \frac{d^2x^2}{dt^2} \tag{28}$$

or, in a simpler expression:

$$E = \ddot{m} \cdot x^2 + \dot{m} \cdot \dot{x^2} + m \cdot \ddot{x^2} \tag{29}$$

Going further and implementing the differentiation on the core term, i.e., $F(m, \vec{x}^2) = m \cdot \vec{x}^2$ (30)

[6],[7],[8], [9], the result is:

$$\frac{d^2}{dt^2}(m \cdot \vec{x}^2) = \frac{d^2m}{dt^2} \cdot \vec{x}^2 + 4 \cdot \frac{dm}{dt} \cdot \vec{x} \cdot \frac{dx}{dt} + 2 \cdot m \cdot \vec{x} \cdot \frac{d^2\vec{x}}{dt^2} + 2 \cdot m \cdot \left(\frac{d\vec{x}}{dt}\right)^2 \tag{31}$$

Then, the energy provided to the mass is expressed as [6],[7],[8],[9]:

$$E = \frac{d^2m}{dt^2} \cdot \vec{x}^2 + 4 \cdot \frac{dm}{dt} \cdot \vec{x} \cdot \frac{dx}{dt} + 2 \cdot m \cdot \vec{x} \cdot \frac{d^2\vec{x}}{dt^2} + 2 \cdot m \cdot \left(\frac{d\vec{x}}{dt}\right)^2 \tag{32}$$

which, in a simpler format, is expressed as [6],[7],[8], [9]:

$$E = \ddot{m}\vec{x}^2 + 4\dot{m}\vec{x} \cdot (\dot{\vec{x}}) + 2m\vec{x} \cdot (\ddot{\vec{x}}) + 2m(\dot{\vec{x}})^2 \tag{33}$$

The derivatives of mass based on relation (23) are [10],[11], [12,][13]:

$$\frac{\mathrm{dm}}{\mathrm{dt}} = \frac{\mathrm{d}}{\mathrm{dt}}\left(\mu_0 e^{i(\omega t+\theta)} - \omega^2\mu_0(C_1' t + C_2')e^{i(\omega t_1+\theta)}\right) \tag{34}$$

or

$$\frac{\mathrm{dm}}{\mathrm{dt}} = \dot{m} = i\omega\mu_0 e^{i(\omega t+\theta)} - \omega^2\mu_0 C_1' e^{i(\omega t_1+\theta)} \tag{35}$$

The second derivative is calculated as:

$$\frac{\mathrm{dm}}{\mathrm{dt}^2} = \frac{\mathrm{d}}{\mathrm{dt}}\left(i\omega\mu_0 e^{i(\omega t+\theta)} - \omega^2\mu_0 C_1' e^{i(\omega t_1+\theta)}\right) \tag{36}$$

or

$$\frac{\mathrm{dm}}{\mathrm{dt}^2} = \ddot{m} = -\omega^2\mu_0 e^{i(\omega t+\theta)} \tag{37}$$

The implementation of the mass differentiation, basis relations (34) up to (37) on equation (33) provides:

$$E = (-\omega^2\mu_0 e^{i(\omega t+\theta)})\vec{x}^2 + 4(i\omega\mu_0 e^{i(\omega t+\theta)} - \omega^2\mu_{0,\varepsilon}C_1' e^{i(\omega t_1+\theta)})\vec{x}\cdot(\dot{\vec{x}}) + 2\mu_0(e^{i(\omega t+\theta)} - \omega^2(C_1' t + C_2')e^{i(\omega t_1+\theta)})((\vec{x}\cdot(\ddot{\vec{x}}) + (\dot{\vec{x}})^2) \quad (38)$$

Since mass is composed of two terms, μ_A and μ_B, it can be considered that the energy can be distributed to these two terms and can be split to E_A and E_B so that each energy term can be assigned to each mass term. Then it is:

$$E_A = -\omega^2\mu_0 e^{i(\omega t+\theta)}\vec{x}^2 + 4i\omega\mu_0 e^{i(\omega t+\theta)}\vec{x}\cdot(\dot{\vec{x}}) + 2\mu_0 e^{i(\omega t+\theta)}((\vec{x}\cdot(\ddot{\vec{x}}) + (\dot{\vec{x}})^2) \quad (39)$$

and

$$E_B = -4\omega^2\mu_0 C_1' e^{i(\omega t_1+\theta)})\vec{x}\cdot(\dot{\vec{x}}) - 2\omega^2\mu_0(C_1' t + C_2')e^{i(\omega t_1+\theta)})((\vec{x}\cdot(\ddot{\vec{x}}) + (\dot{\vec{x}})^2) \quad (40)$$

In the case that two or more masses are added for the creation of a bigger one, the new mass is:

$$m_T = m_{0T}e^{i\varphi_T} \quad (41)$$

so that:

$$m_{0T} = |m_T| = \sqrt{\sum_{i=1}^{n}\mu_{0,i}^2 + 2\sum_{i=1}^{n-1}\sum_{j=i+1}^{n}\mu_{0.i}\mu_{0,j}cos(\theta_i - \theta_i)} \quad (42)$$

and

$$tan\varphi_T = \frac{\sum_{i=1}^{n} sin(\omega_i t) - \sum_{i=1}^{n}\omega_i^2(C'_{1,\iota}t + C'_{2,i})sin(\omega_i t_{1,i})}{\sum_{i=1}^{n} cos(\omega_i t) - \sum_{i=1}^{n}\omega_i^2(C'_{1,\iota}t + C'_{2,i})cos(\omega_i t_{1,i})} \quad (43)$$

In which $n \in \mathbb{N}$ is the total number of masses that contribute to creating the bigger mass and $1 \leq i \leq n$ and $1 \leq j \leq n$.

In such a case, equation (26) becomes:

$$E = \ddot{m}_T\vec{x}^2 + 4\dot{m}_T\vec{x}\cdot(\dot{\vec{x}}) + 2m_T((\vec{x}\cdot(\ddot{\vec{x}}) + (\dot{\vec{x}})^2) \quad (44)$$

Equation (45) is an expanded expression of the energy of a mass at a random position $\vec{x}$ and includes all possible forms of energy of the mass at that position, e.g. kinetic energy, potential energy and forms of energy that are associated with the time-dependent format of mass.

In the case that the mass is considered as a solid object it is:

$$\dot{m}_T = \ddot{m}_T = 0 \quad (45)$$

Then equation (44) turns into:

$$E = 2m_T\vec{x}\cdot(\ddot{\vec{x}}) + 2m_T(\dot{\vec{x}})^2 \quad (46)$$

which of the same format as equation (4).

2.2 Relativistic Approach

The relativity has been developed in order to expand and complete the Newtonia mechanics as there were a number of issues that could be explained by them [14], [15], [16]. In order to make the investigation complete in context, since this paper refers to the quantities of energy, mass, space and time, it is of paramount importance. to include relativistic equations, taking the total energy of a mass as [17], [18], [19]:

$$\mathrm{E} = \gamma \mathrm{m}_0 c^2 \tag{47}$$

so that:

$$\gamma = \frac{1}{\sqrt{1 - \frac{u^2}{c^2}}} \tag{48}$$

where u is the speed of the mass and c is the speed of light.

In this case both the simple format of cem as well the generic format are investigated.

Considering that (47) expresses the total energy of the mass, it can be combined with (39), (40) and (44) and provide the modified equations. In this respect equation (39) is:

$$\mathrm{E_A} = -\omega^2 \mu_0 \mathrm{e}^{\mathrm{i}(\omega t+\theta)} \vec{\mathrm{x}}^2 + 4\mathrm{i}\omega\mu_0 \mathrm{e}^{\mathrm{i}(\omega t+\theta)} \vec{\mathrm{x}} \cdot (\dot{\mathrm{x}}) + 2\mu_0 \mathrm{e}^{\mathrm{i}(\omega t+\theta)} ((\vec{\mathrm{x}} \cdot (\ddot{\vec{x}}) + (\dot{\mathrm{x}})^2) \tag{49}$$

or

$$\mathrm{k_A} \gamma \mathrm{m}_0 c^2 = -\omega^2 \mu_0 \mathrm{e}^{\mathrm{i}(\omega t+\theta)} \vec{\mathrm{x}}^2 + 4\mathrm{i}\omega\mu_0 \mathrm{e}^{\mathrm{i}(\omega t+\theta)} \vec{\mathrm{x}} \cdot (\dot{\mathrm{x}}) + 2\mu_0 \mathrm{e}^{\mathrm{i}(\omega t+\theta)} ((\vec{\mathrm{x}} \cdot (\ddot{\vec{x}}) + (\dot{\mathrm{x}})^2) \tag{50}$$

Whereas equation (33) becomes:

$$\mathrm{E_B} = -4\omega^2 \mu_0 \mathrm{C_1'} \mathrm{e}^{\mathrm{i}(\omega t_1+\theta)}) \vec{\mathrm{x}} \cdot (\dot{\mathrm{x}}) - 2\omega^2 \mu_0 (\mathrm{C_1'} t + \mathrm{C_2'}) \mathrm{e}^{\mathrm{i}(\omega t_1+\theta)}) ((\vec{\mathrm{x}} \cdot (\ddot{\mathrm{x}}) + (\dot{\mathrm{x}})^2) \tag{51}$$

or

$$\mathrm{k_B} \gamma \mathrm{m}_0 c^2 = -4\omega^2 \mu_0 \mathrm{C_1'} \mathrm{e}^{\mathrm{i}(\omega t_1+\theta)}) \vec{\mathrm{x}} \cdot (\dot{\mathrm{x}}) - 2\omega^2 \mu_0 (\mathrm{C_1'} t + \mathrm{C_2'}) \mathrm{e}^{\mathrm{i}(\omega t_1+\theta)}) ((\vec{\mathrm{x}} \cdot (\ddot{\mathrm{x}}) + (\dot{\mathrm{x}})^2) \tag{52}$$

Finally, equation (45) becomes:

$$E = \ddot{m}_T \vec{x}^2 + 4\dot{m}_T \vec{x} \cdot (\dot{\vec{x}}) + 2m_T ((\vec{x} \cdot (\ddot{\vec{x}}) + (\dot{\vec{x}})^2) \tag{53}$$

or

$$\gamma \mathrm{m}_0 c^2 = \ddot{m}_T \vec{x}^2 + 4\dot{m}_T \vec{x} \cdot (\dot{\vec{x}}) + 2m_T ((\vec{x} \cdot (\ddot{\vec{x}}) + (\dot{\vec{x}})^2) \tag{54}$$

considering the total energy of the mass is calculated as per the relativistic approach.

III. RESULTS

When the solutions of equations (39) and (40), derived from the mathematical process, are applied for a single axis $x_i x_i'$ (so that i=1 or 2 or 3 in the case of a 3-dimensional Euclidian space), the general results remain unaltered.

3.1 Analysis of the Results basis the Expanded Energy Modal

The solution of equation (39) provides:

A. Space:

The solution of the differential equation of the real part provides:

$$x_{i,Re}(t) = \pm \frac{\sqrt{-\frac{E_A}{\mu_0}\cos(\omega t + \theta) + k_1 \omega e^{\omega t} + k_2 \omega^2 e^{-\omega t}}}{\sqrt{2}\omega} \tag{55}$$

where:

$$-\frac{E_A}{\mu_0}\cos(\omega t + \theta) + k_1 \omega e^{\omega t} + k_2 \omega^2 e^{-\omega t} \geq 0 \tag{56}$$

and

$$\omega \neq 0 \tag{57}$$

The solution of the differential equation of the imaginary part provides:

$$x_{i,Im}(t) = \pm \frac{\sqrt{\frac{E_A}{\mu_0}\cos(\omega t + \theta) + k_3 \omega^2}}{\sqrt{2}\omega} \tag{58}$$

where:

$$\frac{E_A}{\mu_0}\cos(\omega t + \theta) + k_3 \omega^2 \geq 0 \tag{59}$$

and

$$\omega \neq 0$$

B. Speed:

The differentiation of the relations (55) and (58) yields the speed, which, for equation (55), is calculated as:

$$\dot{x}_{i,Re}(t) = \pm \frac{e^{-\omega t}(\frac{E_A}{\mu_0}\sin(\omega t + \theta)e^{\omega t} + \omega(k_1 e^{2\omega t} - k_2\omega))}{2\sqrt{2}\sqrt{-\frac{E_A}{\mu_0}\cos(\omega t + \theta) + k_1\omega e^{\omega t} + k_2\omega^2 e^{-\omega t}}} \quad (60)$$

with the restriction:

$$-\frac{E_A}{\mu_0}\cos(\omega t + \theta) + k_1\omega e^{\omega t} + k_2\omega^2 e^{-\omega t} > 0 \quad (61)$$

whereas the differentiation of equation (58) provides:

$$\dot{x}_{i,Im}(t) = \mp \frac{\frac{E_A}{\mu_0}\sin(\omega t + \theta)}{\sqrt{\frac{E_A}{\mu_0}\cos(\omega t + \theta) + k_3\omega^2}} \quad (62)$$

where the restriction that applies is:

$$\frac{E_A}{\mu_0}\cos(\omega t + \theta) + k_3\omega^2 > 0 \quad (63)$$

Additionally, the equations that are derived from (58) are:

A. Space:

$$x_{i,Re}(t) = \pm \frac{\sqrt{-\frac{E_B}{2\omega^2\mu_0}cos(\omega t_1 + \theta)\left(C'^2_1 t^2 + C'_1 C'_2 t + C'^2_2\right) + k_4 C'_1 + 2k_5 C'^2_1 (C'_2 t + C'_2)}}{C'_1\sqrt{(C'_1 t + C'_2)}} \quad (64)$$

The restrictions that apply are:

$$-\frac{E_B}{2\omega^2\mu_0}cos(\omega t_1 + \theta)\left(C'^2_1 t^2 + C'_1 C'_2 t + C'^2_2\right) + k_4 C'_1 + 2k_5 C'^2_1 (C'_2 t + C'_2) \geq 0 \quad (65)$$

and

$$C'_1 t + C'_2 > 0 \; and \; C'_1 \neq 0 \quad (66)$$

B. Speed:

$$\dot{x}_{i,Re}(t)$$

$$= \mp \frac{C'_1\left(\frac{E_B}{2\omega^2\mu_0}cos(\omega t_1+\theta)t(C'_1t+C'_2)\right)+k_4}{2(C'_1t+C'_2))^{\frac{3}{2}}\sqrt{-\frac{E_B}{2\omega^2\mu_0}cos(\omega t_1+\theta)\left(C'^2_1t^2+C'_1C'_2t+C'^2_2\right)+C'_1(2k_5C'_1(C'_1t+C'_2)+k_4)}} \quad (67)$$

where the restrictions for this case are:

$$-\frac{E_B}{2\omega^2\mu_0}cos(\omega t_1+\theta)\left(C'^2_1t^2+C'_1C'_2t+C'^2_2\right)+C'_1(2k_5C'_1(C'_1t+C'_2)+k_4)>0 \quad (68)$$

or

$$C'_1t+C'_2>0$$

Equation (40) provides solutions only from the real part, while the solutions derived from the imaginary part of equation (40) define a point or set of points where this relation applies. These can be expressed as follows:

1. in case $\omega \neq 0$, then $t_1=\frac{n\pi}{\omega}-\frac{\theta}{\omega},\ n\epsilon\mathbb{Z}$ (69)

2. in case $\omega=0$, then $t_1=n\pi,\ n\epsilon\mathbb{Z}$, which is not the case since it is desired that $\omega\neq 0$ (70)

To combine equations with (56) and (51) with (59), it is considered that:

$$E=E_A+E_B \quad (71)$$

It can be set:

$$E_A=k_EE \quad (72)$$

and

$$E_B=(1-k_E)E \quad (73)$$

so that the factor k_E:

$$k_E\in[0,1]\subset\mathbb{R} \quad (74)$$

expresses how energy is distributed between the two parts of mass.

In addition, the quantity E expresses the total energy supplied to the mass.

The combination of equations (71) up to (74) with (55), (58), (52), (54), (56) and (59) provide the following results:

Space: The solution of the real part provides two terms, each affecting the change of space depending on the time and energy supplied to the mass. In this respect, the equation that expresses the space is the sum of both terms on each axis. Taking into consideration the equations (54) and (66) in combination with (62) and (63), the expressions of space are derived as follows:

For the real part:

$$x_{i,Re}(E,t) = \pm\frac{\sqrt{-\frac{k_E E}{\mu_0}\cos(\omega t+\theta)+k_1\omega e^{\omega t}+k_2\omega^2 e^{-\omega t}}}{\sqrt{2}\omega} \pm\frac{\sqrt{-\frac{(1-k_E)E}{2\omega^2\mu_0}cos(\omega t_1+\theta)\left(C'^2_1 t^2+C'_1C'_2 t+C'^2_2\right)+k_4C'_1+2k_5C'^2_1(C'_2 t+C'_2)}}{\sqrt{C'^2_1(C'_1 t+C'_2)}} \quad (75)$$

For the imaginary part:

$$x_{i,Im}(E,t) = \pm\frac{\sqrt{\frac{k_E E}{\mu_0}\cos(\omega t+\theta)+k_3\omega^2}}{\sqrt{2}\omega} \quad (76)$$

Speed: The solution of the real part provides two terms, each depending on time and energy. In this respect, the equations that express speed are the sum of both terms on each axis. Taking into consideration the equations (63) and (66), in combination with (61) and (72), the expressions of speed yielded as follows:

Real part:

$$\dot{x}_{i,Re}(t) = \pm\frac{\frac{k_E E}{\mu_0}\sin(\omega t+\theta)+k_1\omega e^{\omega t}-k_2\omega^2 e^{-\omega t}}{2\sqrt{2}\sqrt{-\frac{k_E E}{\mu_0}\cos(\omega t+\theta)+k_1\omega e^{\omega t}+k_2\omega^2 e^{-\omega t}}} \mp\frac{C'_1\left(\frac{(1-k_E)E}{2\omega^2\mu_0}cos(\omega t_1+\theta)t(C'_1 t+2C'_2)+k_4\right)}{2(C'_1 t+C'_2))^{\frac{3}{2}}\sqrt{-\frac{(1-k_E)E}{2\omega^2\mu_0}cos(\omega t_1+\theta)\left(C'^2_1 t^2+C'_1C'_2 t+C'^2_2\right)+C'_1(2k_5C'_1(C'_1 t+C'_2)+k_4)}} \quad (77)$$

Imaginary part:

$$\dot{x}_{i,Im}(t) = \mp \frac{\frac{k_E E}{\mu_0} \sin(\omega t + \theta)}{2\sqrt{\frac{k_E E}{\mu_0} \cos(\omega t + \theta) + k_3 \omega^2}} \tag{78}$$

The mathematical process for the solution of equation (44) is more complicated, and various solutions have been proposed. One of the solutions proposed considers $\theta = p_1 t + p_2$.

Again, for the solution of this equation, it is assumed that the use of a single axis does not affect the generality of the results; in this case, the study focuses on the axis $x_i x_i'$. The equations that express space are:

Real part:

$$x_{i,Re}(t) = \pm \frac{\sqrt{-\frac{E}{m_{0T}} \cos(p_1 t + p_2) + p_3 p_1 e^{p_1 t} + p_4 p_1^2 e^{-p_1 t}}}{\sqrt{2} p_1} \tag{79}$$

where the applicable restrictions are:

$$-\frac{E}{m_{0T}} \cos(p_1 t + p_2) + p_3 p_1 e^{p_1 t} + p_4 p_1^2 e^{-p_1 t} \geq 0 \tag{80}$$

and

$$p_1 \neq 0 \tag{81}$$

Imaginary part:

$$x_{i,Im}(t) = \pm \frac{\sqrt{\frac{E}{m_{0T}} \cos(p_1 t + p_2) + p_5 {p_1}^2}}{\sqrt{2} p_1} \tag{82}$$

where the restrictions are:

$$\frac{E}{m_{0T}} cos(p_1 t + p_2) + p_5 {p_1}^2 \geq 0 \tag{83}$$

and

$$p_1 \neq 0$$

The equations of speed that are produced from the equation (82) is:

$$\dot{x}_{i,Im}(t) = \mp \frac{\frac{E}{m_{0T}} \sin(p_1 t + p_2)}{2\sqrt{\frac{E}{m_{0T}} \cos(p_1 t + p_2) + p_5 {p_1}^2}} \tag{84}$$

having as restriction:

$$\frac{E}{m_{0T}} cos(p_1 t + p_2) + p_5 {p_1}^2 > 0 \tag{85}$$

Whereas the speed that is produced from equation (79) is:

$$\dot{x}_{i,Re}(\mathrm{t}) = \pm \frac{\frac{E}{m_{0T}} \sin(p_1 t + p_2) + p_3 p_1 \mathrm{e}^{p_1 \mathrm{t}} - p_4 p_1^2 \mathrm{e}^{-p_1 \mathrm{t}}}{2\sqrt{2}\sqrt{-\frac{E}{m_{0T}} \cos(p_1 t + p_2) + p_3 p_1 \mathrm{e}^{p_1 \mathrm{t}} + p_4 p_1^2 \mathrm{e}^{-p_1 \mathrm{t}}}} \tag{86}$$

The applicable restriction is:

$$-\frac{E}{m_{0T}} \cos(p_1 t + p_2) + p_3 p_1 \mathrm{e}^{p_1 \mathrm{t}} + p_4 p_1^2 \mathrm{e}^{-p_1 \mathrm{t}} > 0 \tag{87}$$

The equations (75), (76), (77), (78), as well as (79), (82), (84) and (86), are represented by the figures below, using energy and time as parameters.

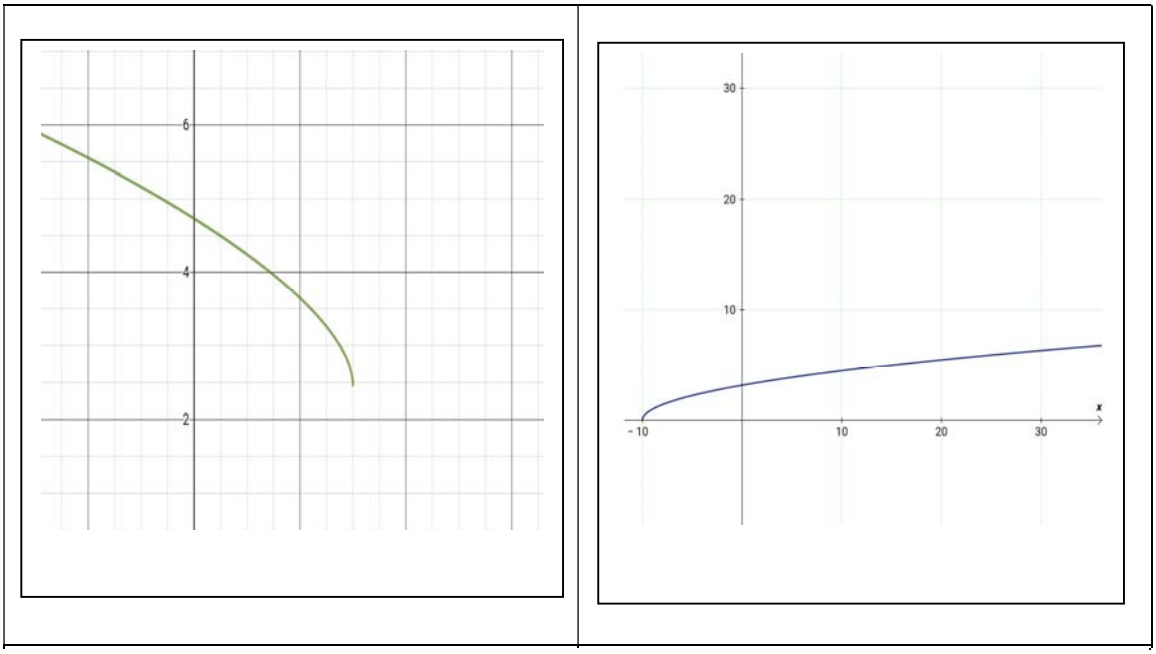

Figure 1: Graphical representation of real part of space dependent on energy based on equation (75)

Figure 2: Graphical representation of imaginary part of space dependent on energy based on equation (76)

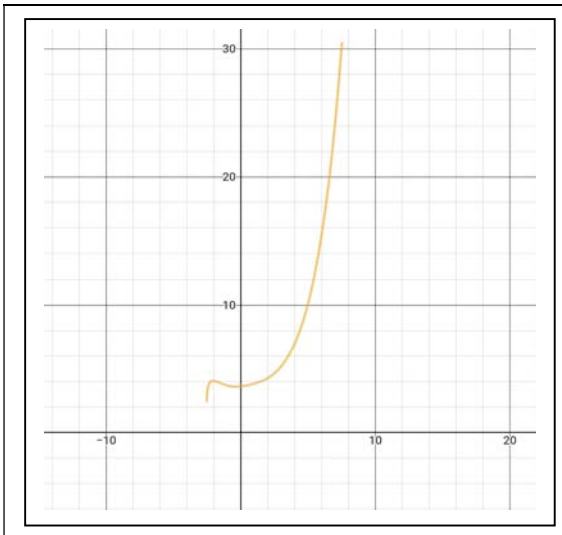

Figure 3: Graphical representation of real part of space dependent on time, based on equation (75)

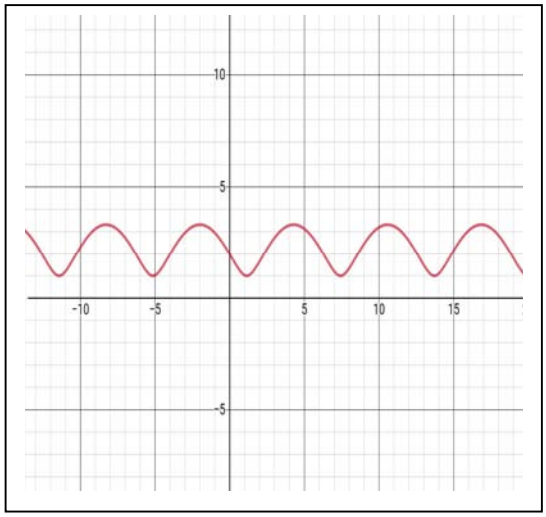

Figure 4: Graphical representation of imaginary part of space dependent on time, based on equation (76)

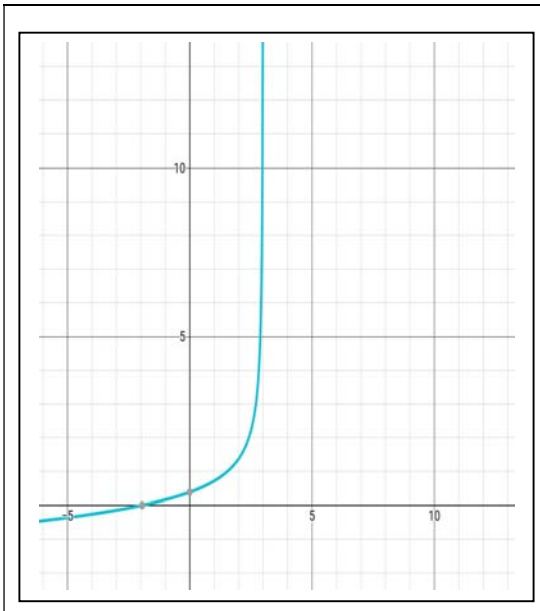

Figure 5: Graphical representation of the real part of speed dependent on energy based on equation (77)

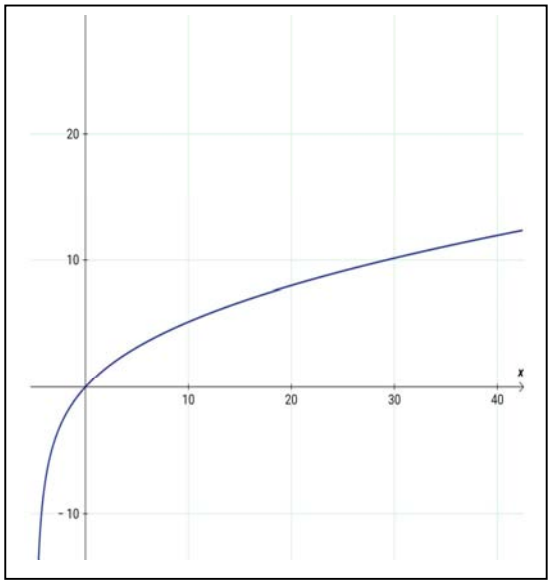

Figure 6: Graphical representation of imaginary part of speed dependent on energy based on equation (78)

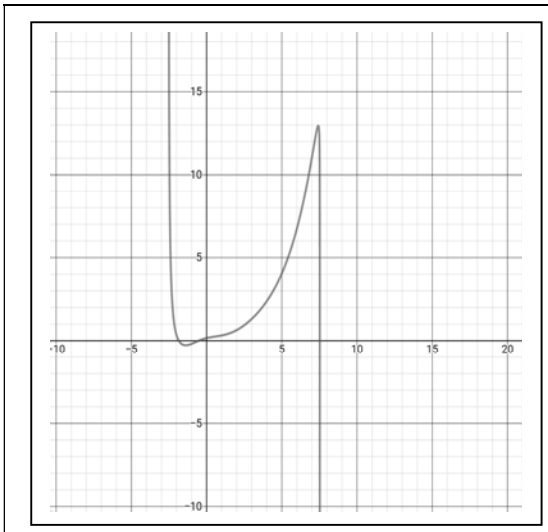

Figure 7: Graphical representation of the real part of speed dependent on time, based on equation (77)

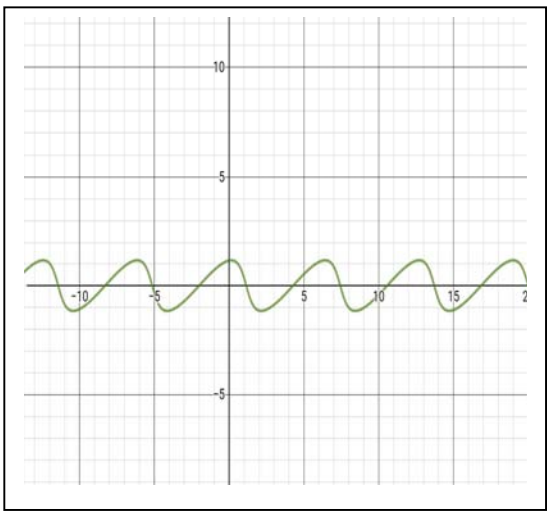

Figure 8: Graphical representation of imaginary part of speed dependent on time, based on equation (78)

In addition to the above, the results of the generic equations are presented here below:

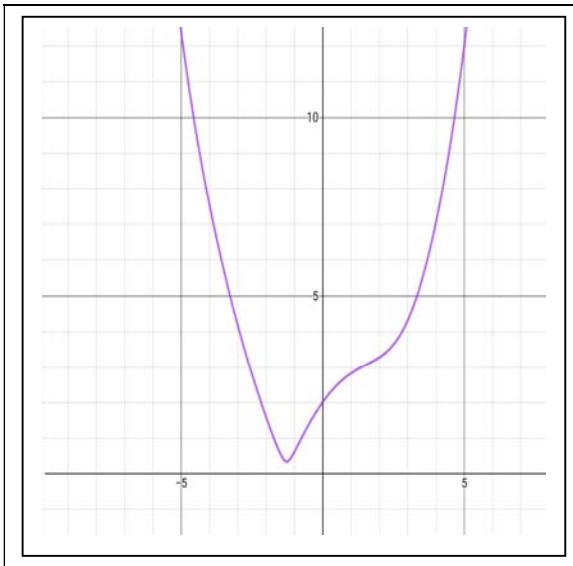

Figure 9: Graphical representation of generic real part of space dependent on time, based on equation (79)

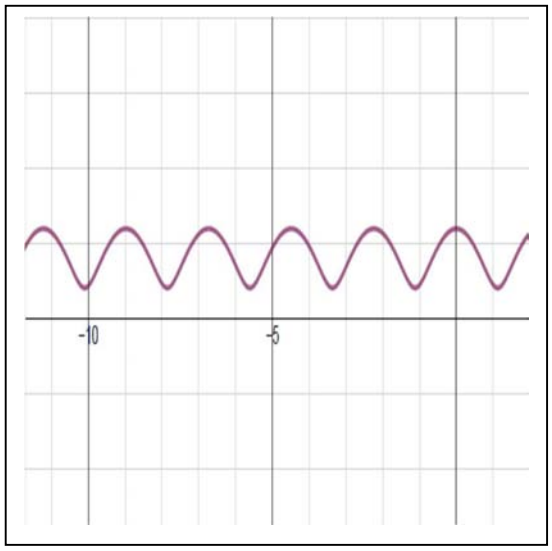

Figure 10: Graphical representation of generic imaginary part of space dependent on time, based on equation (82)

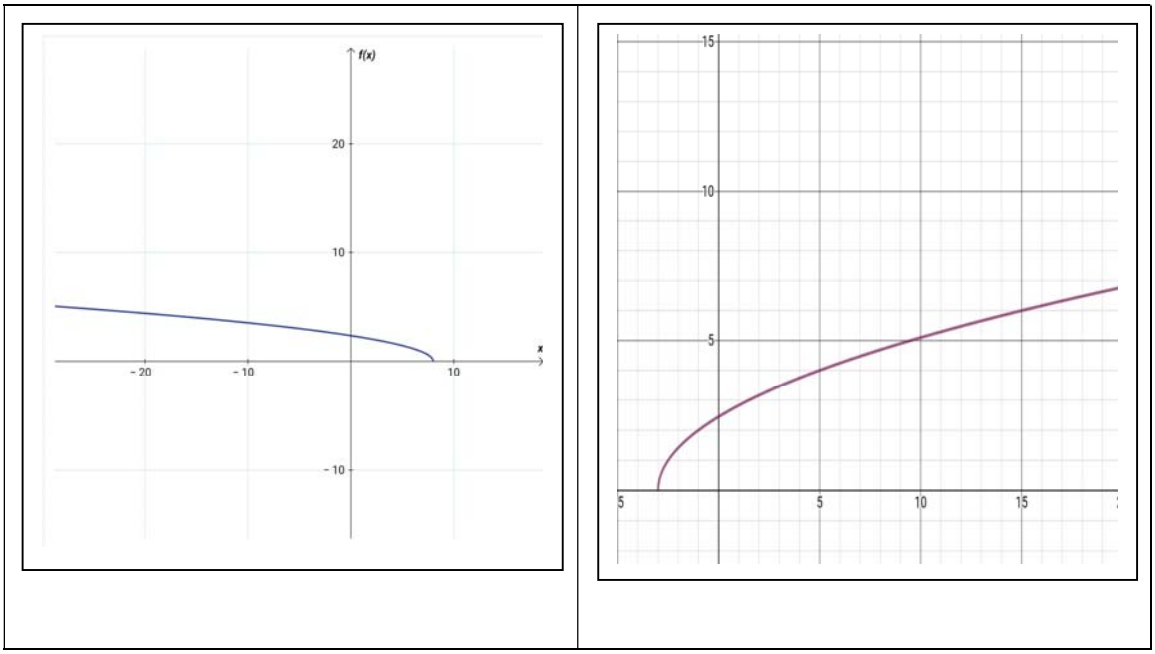

Figure 11: Graphical representation of generic real part of space dependent on energy based on equation (79)

Figure 12: Graphical representation of generic imaginary part of space dependent on energy based on equation (82)

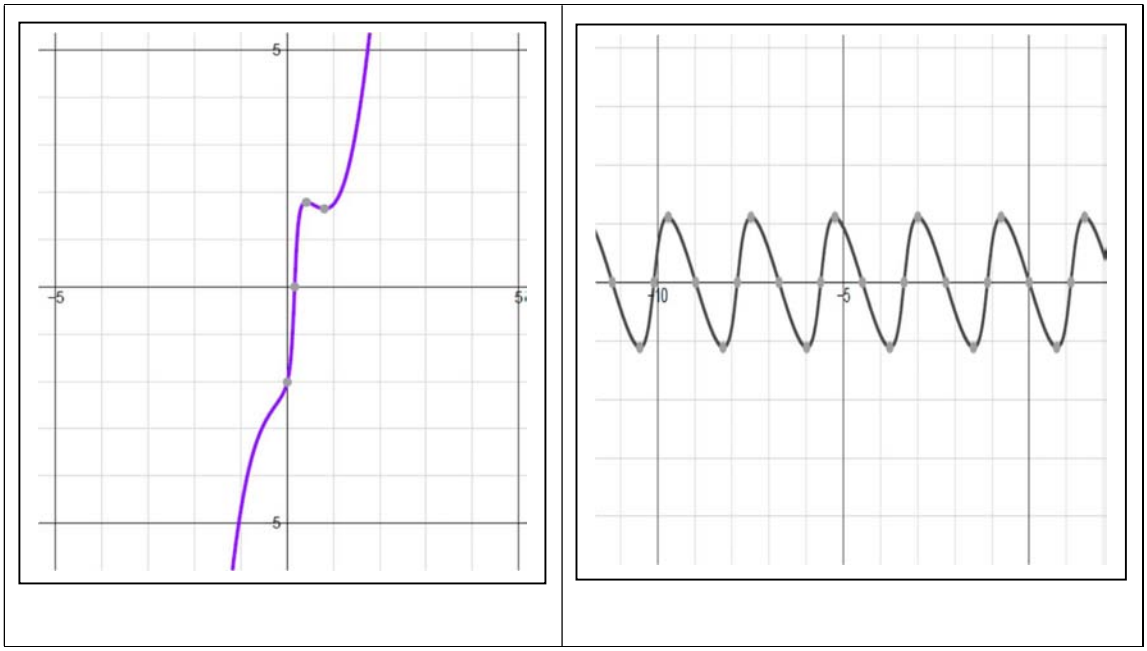

Figure 13: Graphical representation of generic real part of speed dependent on time, based on equation (86)

Figure 14: Graphical representation of generic imaginary part of speed dependent on time, based on equation (84)

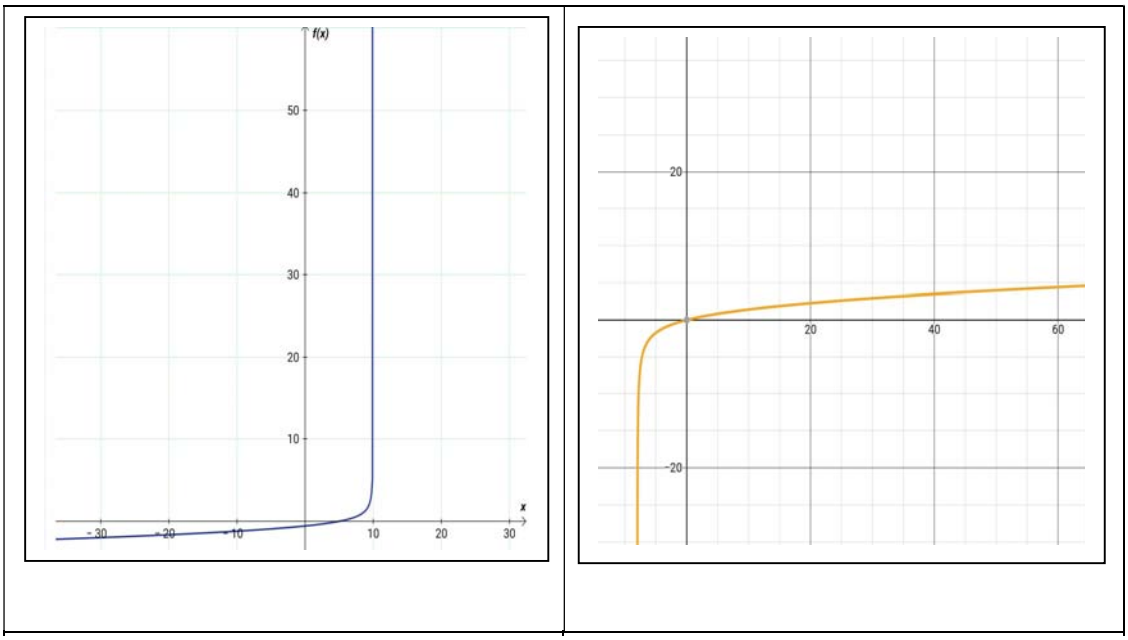

Figure 15: Graphical representation of generic real part of speed dependent on energy based on equation (86)

Figure 16: Graphical representation of generic imaginary part of speed dependent on energy based on equation (84)

The equations developed reveal that space and speed are interconnected with both energy and time. To investigate how space and speed change simultaneously with respect to energy and time, the following three-dimensional graphs have been developed, assigning energy to the x-axis and time to the y-axis. In all these graphs, time has been considered to be equal to or greater than zero ($t \geq 0$) based on the causational law.

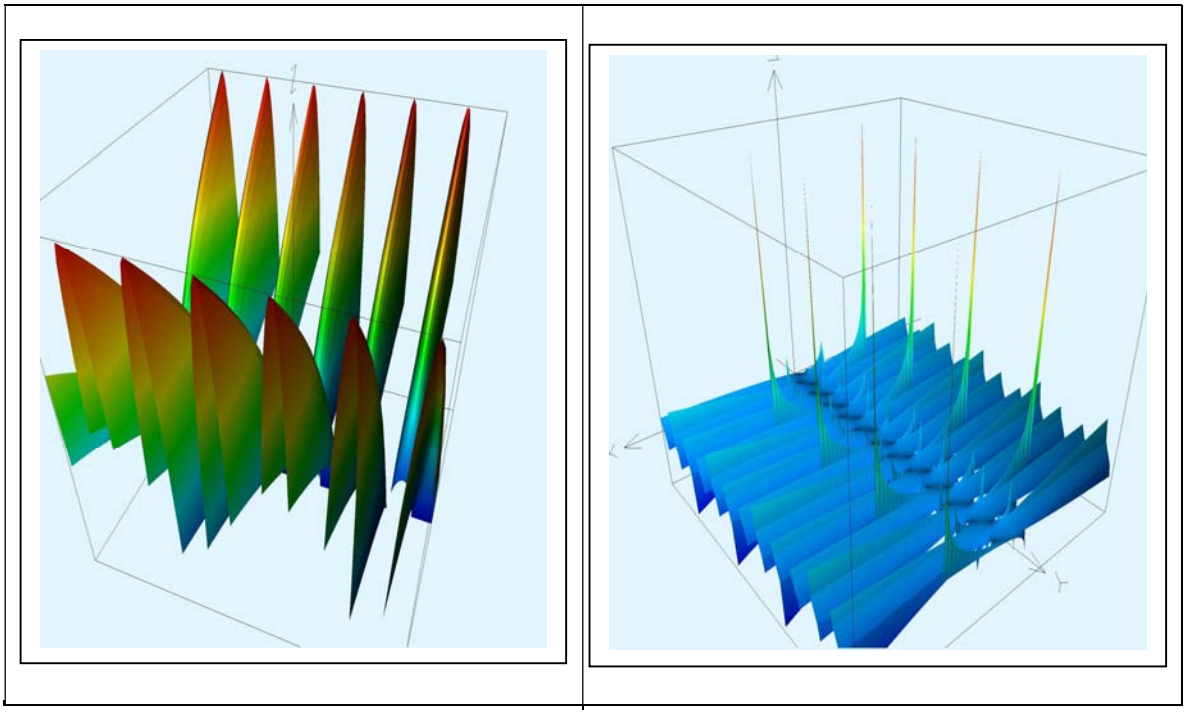

Figure 17: 3-dimensional representation of equation (76)

Figure 18: 3-dimensional representation of equation (78)

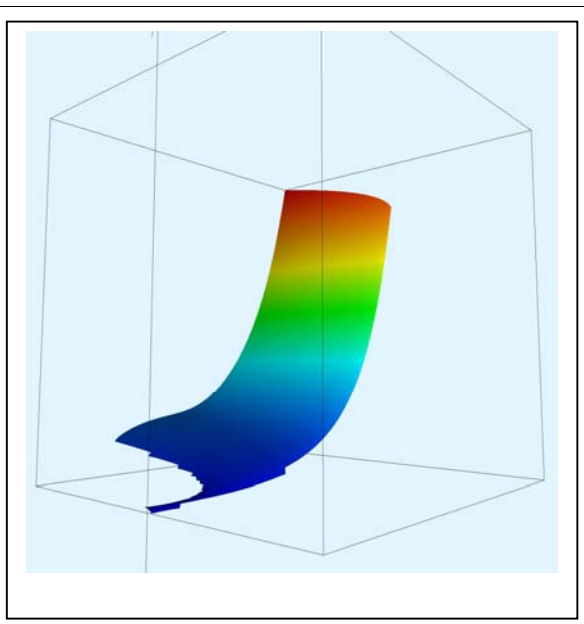

Figure 19: 3-dimensional representation of equation (75)

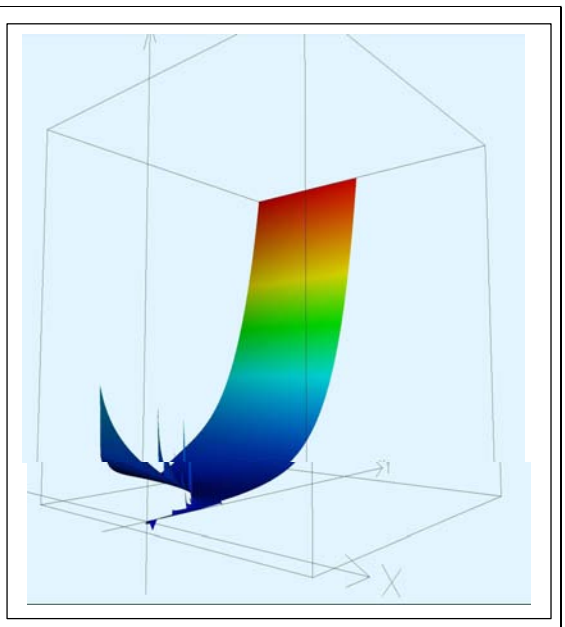

Figure 20: 3-dimensional representation of equation (77)

Representation of the generic equations on three dimensions:

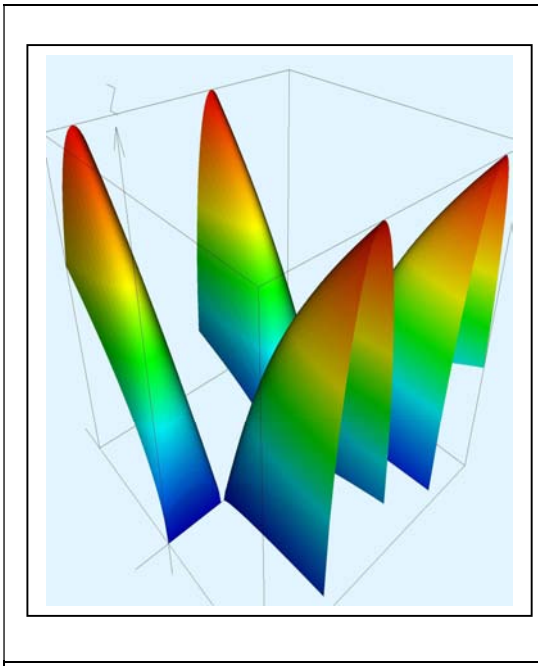

Figure 21: 3-dimensional representation of equation (82)

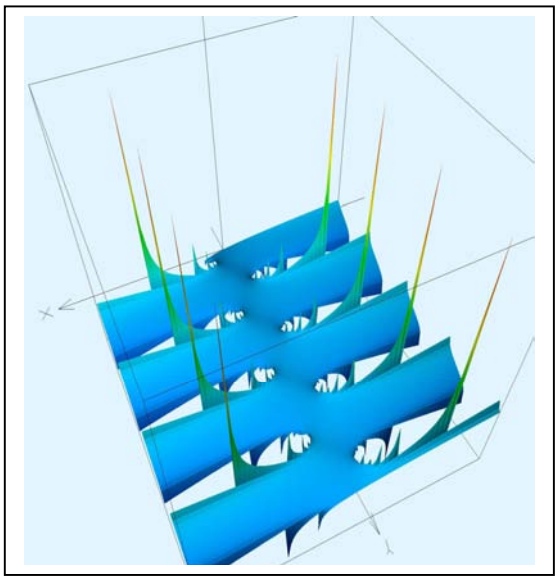

Figure 22: 3-dimensional representation of equation (84)

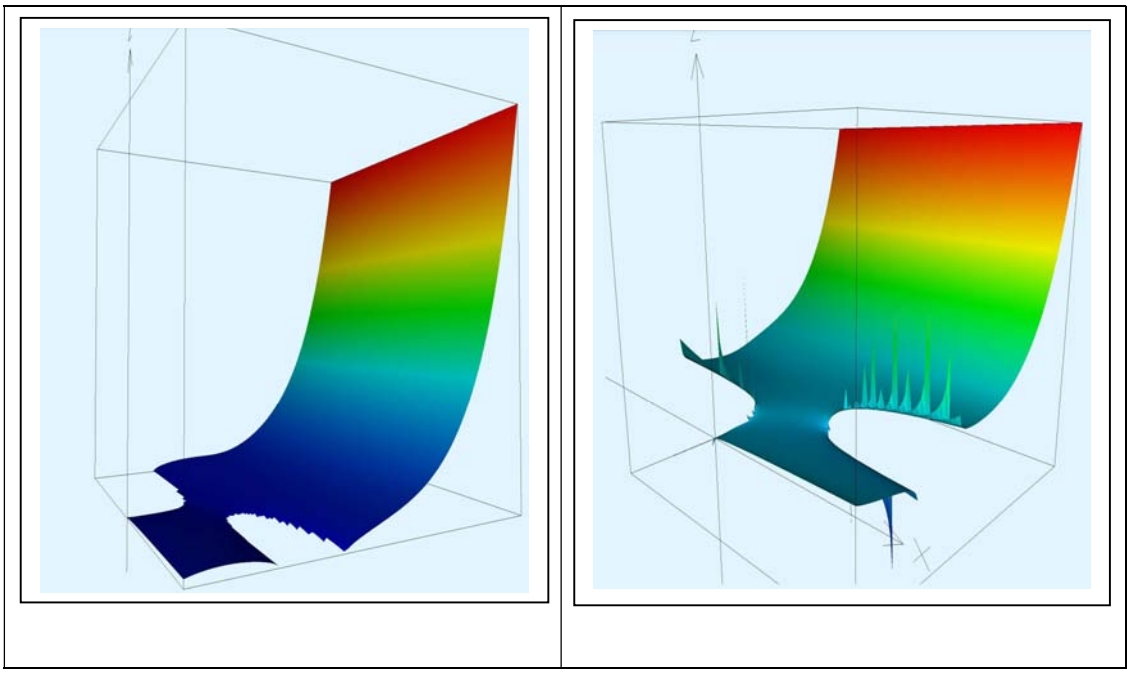

Figure 23: 3-dimensional representation of equation (79)

Figure 24: 3-dimensional representation of equation (86)

The analysis of the constraints that are described in equations (56), (59), (57), (61), (63), (65), (66), and (68) applies to the pem, whereas for a formed mass the relevant equations include (80), (81), (83), (86) and (87). The equations that satisfy all the constraints are equations (61), (63), (68) and (87). The following figures represent equations (61), (63) and (68).

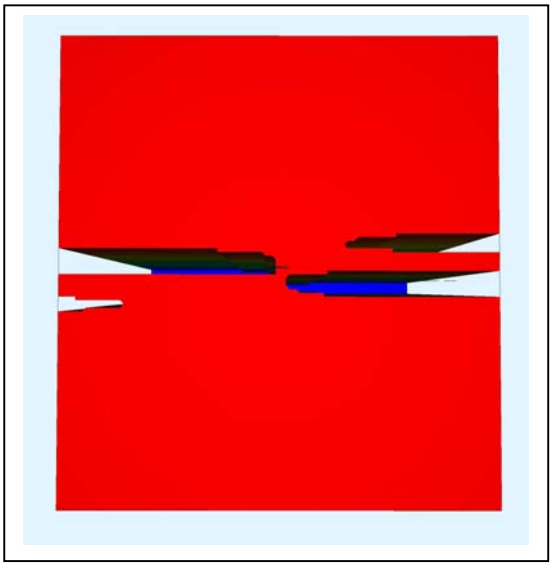

Figure 25: E-t plane that equation (61) is valid

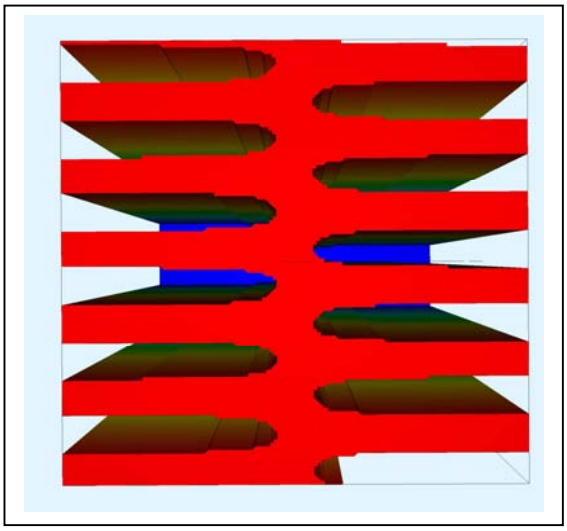

Figure 26: E-t plane that equation (63) is valid

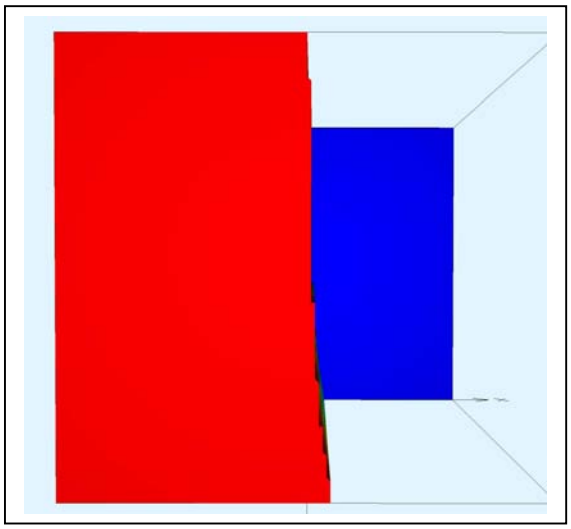

Figure 27: E-t plane that equation (68) is valid

The areas presented in these graphs indicate the areas where the equations yield real solutions. However, special emphasis must be given to the boundary lines separating the areas where equations are valid (red-colored areas) from those where the equations are invalid (blue-colored areas). The pairs of values of energy and time on these boundary lines correspond to points where denominators attain the level of zero, leading the equations that express speed to incline towards infinity. As is expected, if mass reaches the limit values of these constraints, it can maximize the speed and consequently minimize the space.

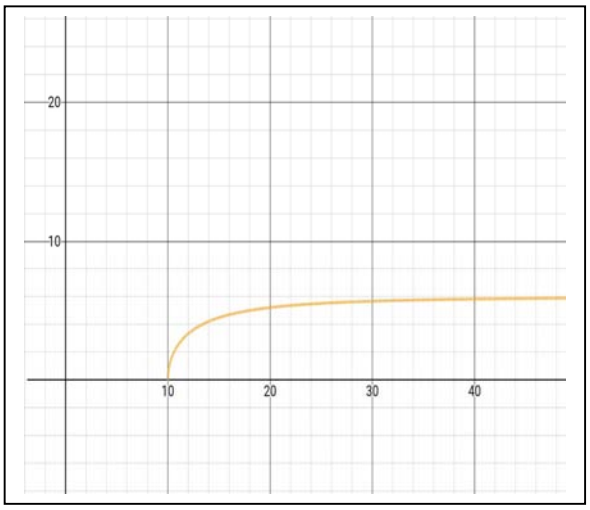

Figure 28: Representation of equation (88) speed vs energy

Equation (50) by the use of equation (72) turns into:

$$k_E\gamma c^2 = -\omega^2 e^{i(\omega t+\theta)}x_i^2 + 4i\omega e^{i(\omega t+\theta)}x_i\cdot(\dot{x_\iota}) + 2e^{i(\omega t+\theta)}\left(x_i\cdot(\ddot{x_\iota}) + (\dot{x_\iota})^2\right) \quad (89)$$

or

$$k_E\gamma c^2 e^{i(-(\omega t+\theta))} = -\omega^2 x_i^2 + 4i\omega x_i\cdot(\dot{x_\iota}) + 2\left(x_i\cdot(\ddot{x_\iota}) + (\dot{x_\iota})^2\right) \quad (90)$$

If the parameter γ is considered as a constant dependent on speed then (90) turns into:

Real Part:

$$k_E\gamma c^2\cos(-(\omega t+\theta)) = -\omega^2 x_i^2 + 2x_i\cdot(\ddot{x_\iota}) + 2(\dot{x_\iota})^2 \quad (91)$$

Imaginary Part:

$$k_E\gamma c^2\sin(-(\omega t+\theta)) = 4\omega x_i\cdot(\dot{x_\iota}) \quad (92)$$

In addition, equation (52), with the use of equation (73), turns into:

$$(1-k_E)\gamma c^2 = -2\omega^2 C_1' e^{i(\omega t_1+\theta)}x_i\cdot(\dot{x_\iota}) - 2\omega^2(C_1' t + C_2')e^{i(\omega t_1+\theta)}\left(x_i\cdot(\ddot{x_\iota}) + (\dot{x_\iota})^2\right) \quad (93)$$

or

$$-\frac{(1-k_E)\gamma c^2}{2\omega^2}e^{i(-(\omega t_1+\theta))} = C_1' x_i\cdot(\dot{x_\iota}) + (C_1' t + C_2')\left(x_i\cdot(\ddot{x_\iota}) + (\dot{x_\iota})^2\right) \quad (94)$$

The real and imaginary parts of which are:

Real part:

$$-\frac{(1-k_E)c^2}{2\omega^2}\gamma\cos(-(\omega t_1+\theta))=\left(C_1'x_i\cdot(\dot{x_\iota})+(C_1't+C_2')\left(x_i\cdot(\ddot{x_\iota})+(\dot{x_\iota})^2\right)\right) \quad (95)$$

Imaginary part:

$$-\frac{(1-k_E)c^2}{2\omega^2}\gamma\sin(-(\omega t_1+\theta))=0 \quad (96)$$

Finally, equation (44) turns into:

$$\gamma c^2 = (i\ddot{\vartheta}-\dot{\vartheta}^2)e^{i\vartheta}x_i^2+4i\dot{\vartheta}x_i\cdot(\dot{x_\iota})e^{i\vartheta}+2(x_i\cdot(\ddot{x_\iota})+(\dot{x_\iota})^2)e^{i\vartheta} \quad (97)$$

or

$$\gamma c^2\, e^{-i} = (i\ddot{\vartheta}-\dot{\vartheta}^2)x_i^2+4i\dot{\vartheta}x_i\cdot(\dot{x_\iota})+2\left(x_i\cdot(\ddot{x_\iota})+(\dot{x_\iota})^2\right) \quad (98)$$

provided that:

$$m_0=m_T \quad (99)$$

or

$$m_0=g_\varepsilon g_t g_{\bar{s}}' \quad (100)$$

Equation (94) is separated to real and imaginary parts as follows:

Real Part:

$$\gamma c^2\cos(-\vartheta)=-\dot{\vartheta}^2x_i^2+2x_i\cdot(\ddot{x_\iota})+2(\dot{x_\iota})^2 \quad (101)$$

Imaginary Part:

$$\gamma c^2\sin(-\vartheta)=\ddot{\vartheta}x_i^2+4\dot{\vartheta}x_i\cdot(\dot{x_\iota}) \quad (102)$$

In all equations of this section the common characteristic is the lack of energy and mass from any part. This means that the solution of the differential equations relates space with time.

considering $m_0=\mu_0$ and that the calculations are carried out on axis i.

The solution of the equations (83), (84) and (95) are as follows:

$$x_{i,Re}(E,t) = \pm\frac{\sqrt{-k_E\frac{c^3}{\sqrt{c^2-u^2}}\cos(\omega t+\theta)+k_1\omega e^{\omega t}+k_2\omega^2 e^{-\omega t}}}{\sqrt{2}\omega} \quad (103)$$

For the imaginary part:

$$x_{i,Im}(u,t) = \pm\frac{\sqrt{k_E\frac{c^3}{\sqrt{c^2-u^2}}\cos(\omega t+\theta)+k_3\omega^2}}{\sqrt{2}\omega} \quad (104)$$

$$x_{i,Re}(u,t) = \pm\frac{\sqrt{-\frac{(1-k_E)}{2\omega^2}\frac{c^3}{\sqrt{c^2-u^2}}cos(\omega t_1+\theta)\left(C'^2_1t^2+C'_1C'_2t+C'^2_2\right)+k_4C'_1+2k_5C'^2_1(C'_2t+C'_2)}}{C'_1\sqrt{(C'_1t+C'_2}} \quad (105)$$

The combination of the equations (103) and (105) provide:

$$x_{i,Re}(u,t) = \pm\frac{\sqrt{-k_E\frac{c^3}{\sqrt{c^2-u^2}}\cos(\omega t+\theta)+k_1\omega e^{\omega t}+k_2\omega^2 e^{-\omega t}}}{\sqrt{2}\omega} \pm\frac{\sqrt{-\frac{(1-k_E)}{2\omega^2}\frac{c^3}{\sqrt{c^2-u^2}}cos(\omega t_1+\theta)\left(C'^2_1t^2+C'_1C'_2t+C'^2_2\right)+k_4C'_1+2k_5C'^2_1(C'_2t+C'_2)}}{C'_1\sqrt{(C'_1t+C'_2}} \quad (106)$$

Which expresses the real part of space connected to time and speed, considering γ as:

$$\gamma = \frac{c}{\sqrt{c^2-u^2}} \quad (107)$$

The solution of (97) and (98), provide the following solutions:

$$x_{i,Re}(u,t) = \pm\frac{\sqrt{-\frac{c^3}{\sqrt{c^2-u^2}}\cos(p_1t+p_2)+p_3p_1e^{p_1t}+p_4p_1^2e^{-p_1t}}}{\sqrt{2}p_1} \quad (108)$$

and

$$x_{i,Im}(u,t) = \pm\frac{\sqrt{\frac{c^3}{\sqrt{c^2-u^2}}\cos(p_1 t + p_2) + p_5 {p_1}^2}}{\sqrt{2}p_1} \quad (109)$$

considering: $\vartheta = p_1 t + p_2$

It is noticed that in equations (103), (104) and (105) the time and space are connected directly without the use of energy or mass, but this is expected since the total energy of the mass has been replaced by the equation (47).

IV. DISCUSSION

The equations that have been developed so far indicate that space and speed are functions of energy and time. The behavior of space and speed are analyzed in a mathematical way, producing corresponding equation, followed by a comparison of the dependence on energy, since the equations developed indicate a direct relation between these three quantities. Equations deriving from the relativistic expression of energy are used to carry out a complete investigation that includes speed.

4.1 Analysis of the Speed Equations

This paragraph examines the equations of speed deriving from equation (38), which is expressed in the set of complex numbers, starting with those that are described by the imaginary part this equation. The analysis describes the change and possible limitations of speed related to energy and compares the equation with the basic expression of speed, as expressed in equation (2), and expands to the use of the relativistic models and equations.

4.1.1 The Analysis of the Imaginary Part of the Speed Equations

The widely used expression of kinetic energy is $E_k = \frac{1}{2}mu^2$, so the expression of speed depending on energy is:

$$u = \pm\sqrt{\frac{2E_k}{m}}, m \neq 0 \quad (110)$$

The study of equation (45), depending on energy, reveals a similarity to the equation

$$f(y) = k_y\sqrt{y} \quad (111)$$

with $k_y \epsilon \mathbb{R}$, given a specific value of time. This is the same format that aligns with equation (110). The difference between (78) and the speed equation (110) lies in the term $r_1 = \mathrm{k}_3\omega^2$ and the trigonometric terms. In the case where the factor k_3 is equal to zero, i.e., $\mathrm{k}_3 = 0$, it receives the format as follows:

$$\dot{x}(\mathrm{E}) = \sqrt{\frac{k_E \mathrm{E}}{\mu_0}\cos(\omega \mathrm{t} + \theta)} \cdot \tan(\omega \mathrm{t} + \theta) \tag{112}$$

This format is of the same type as equation (110) or (111), considering a specific value of time. Another difference between equations (78) and (110) is that equation (110) does not mention any explicit reference to time, which is why equation (78) is considered more comprehensive.

The restrictions that apply to equation (78) are:

$$\frac{k_E \mathrm{E}}{\mu_0}\cos(\omega \mathrm{t} + \theta) + \mathrm{k}_3\omega^2 > 0 \tag{113}$$

Finally, equation (110) shares structural similarities with (78) and (84), which means that both (78) and (84) express speed in an expanded way compared to the typical expression of speed, depending on energy. Notably, both these equations are the results of the solution of the imaginary components of (38) and (44), respectively. Figure 29 shows the representation of (78), (84), and (110) in graphical format. The same figure also includes the representation of equation (88) which represents the change of speed over the relativistic total energy.

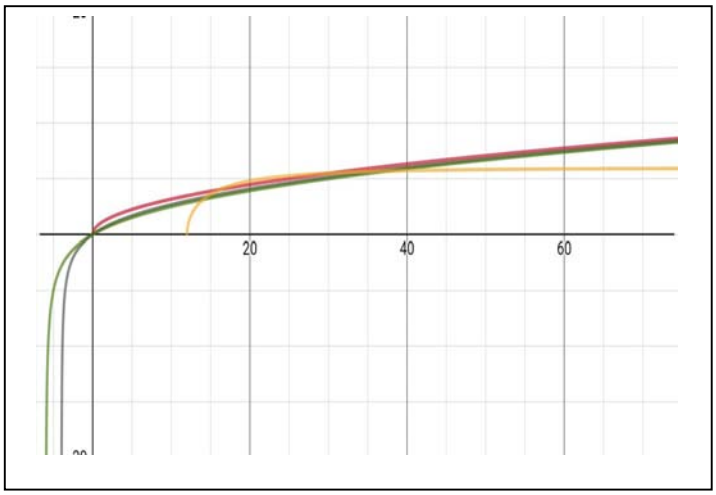

Figure 29: Graphical presentation of equations (78), (84), (88) and (110)

Black line presents equation (78)

Green line presents equation (84)

Yellow line represents equation (88)

Red line presents equation (100)

While investigating the potential limitations of speed, it is important to find the limit of these equations as energy moves to infinity. In such a case, the limit of (78) as energy tends towards infinity is:

$$\lim_{E\to+\infty} \dot{x}(t) = \lim_{E\to+\infty} \frac{\frac{\mathrm{E}}{\mu_0}\sin(\omega t+\theta)}{2\sqrt{\frac{\mathrm{E}}{\mu_0}\cos(\omega t+\theta)+k_3\omega^2}} \tag{114}$$

or

$$\lim_{E\to+\infty} \dot{x}(t) = \lim_{E\to+\infty} \frac{\frac{\mathrm{E}}{\mu_0}\sin(\omega t+\theta)\sqrt{\frac{\mathrm{E}}{\mu_0}\cos(\omega t+\theta)+k_3\omega^2}}{2\left(\frac{\mathrm{E}}{\mu_0}\cos(\omega t+\theta)+k_3\omega^2\right)} = \infty \tag{115}$$

In addition, the limit of (84) as energy tends towards infinity is:

$$\lim_{E\to+\infty} \dot{x}(t) = \lim_{E\to+\infty} \frac{\frac{E}{m_{0T}}\sin(p_1 t+p_2)}{2\sqrt{\frac{E}{m_{0T}}\cos(p_1 t+p_2)+p_5{p_1}^2}} = \infty \tag{116}$$

The outcome of this analysis is that, considering only these equations, there is no apparent limitation for the value of speed, as energy tends to infinity.

On the other hand, a certain combination of values of time and energy may lead the denominator in these equations to approach zero, i.e.:

$$\frac{E_1}{m_{0T}}cos(p_1 t_1+p_2)+p_5{p_1}^2 = 0 \tag{117}$$

wherein the speed tends to infinity, i.e.

$$\lim_{E\to E_1} \frac{\frac{\mathrm{E}}{\mu_0}\sin(\omega t_1+\theta)}{2\sqrt{\frac{\mathrm{E}}{\mu_0}\cos(\omega t_1+\theta)+k_3\omega^2}} = \infty \tag{118}$$

However, this pair of values does not affect the format of equations (78), (84), and (110) expressed in graphs, as energy tends to infinity.

The use of relativistic mechanics describes the total energy of a mass by the relation (47) whereas the speed, if calculated from this model, results in equation (110).

Of course, in relativistic mechanics, it is taken axiomatically that the maximum speed a mass can reach is that of light (c) which is also objective for all bodies [20], [21], [22].

If we compare the relations (110) and the relation (111) with the relations (782) and (82) which results from the analysis of the imaginary part of the energy, similarities are observed. The expression of the speed through the relation (88) shows the limit set by the relative axiom. Although the equations (78), (84) and (110) show that the speed does not tend to some given value, the axiom of relativistic mechanics could also apply in the case of the imaginary part of this model.

4.1.2 Analysis of The Real Part of Speed - Differentiation towards Other Models

The two models of classical and relativistic physics, consider mass as a given state. The differentiation of this work lies in the consideration of mass as a dynamic quantity. The result of this differentiation in combination with the expression of mass through the wide magnitude of complex numbers allows the expression of velocity with an additional term, shown in the relations (78) and (84). Therefore, if it is assumed that the limitation of velocity to the speed of light applies to the expression of the imaginary part in the relations (78) and (84), in the real part this does not seem to have any effect, as shown in the relations (77) and (79).

Equations (75) and (86), depending on energy, as presented in Figure 1 and Figure 15, respectively, reveal a value of energy specific for each equation, which, when attained, mass can travel at infinite speed, given a specific time value. This can be expressed for equation (108) as follows:

$$\lim_{E\to E_l}\dot{x}_{i,Re}(\mathrm{t})=\lim_{E\to E_l}\frac{\frac{E}{m_{0T}}\sin(p_1t_1+p_2)+p_3p_1\mathrm{e}^{pt_1}-p_4p_1^2\mathrm{e}^{-p_1t_1}}{2\sqrt{2}\sqrt{-\frac{E}{m_{0T}}\cos(p_1t_1+p_2)+p_3p_1\mathrm{e}^{p_1t_1}+p_4p_1^2\mathrm{e}^{-p_1t_1}}}=\infty \tag{119}$$

where t_1 is a specific time value, and E_l is the value of energy that can zero the denominator, and when the energy approaches this value, then speed tends to infinity. This value can be calculated as follows:

$$-E_l\frac{1}{m_{0T}}\cos(p_1t_1+p_2)+p_3p_1\mathrm{e}^{p_1t_1}+p_4p_1^2\mathrm{e}^{-p_1t_1}=0 \tag{120}$$

or

$$E_l=m_{0T}\frac{p_3p_1\mathrm{e}^{p_1t_1}+p_4p_1^2\mathrm{e}^{-p_1t_1}}{\cos(p_1t_1+p_2)},\cos(p_1t_1+p_2)\neq 0 \tag{121}$$

This expression could lead to an investigation of the way in which energy could be distributed in the mass so that it moves at a speed, possibly, greater than that of light. An example is the division of total energy into energy and exergy. Also, in many systems there is active and inactive power. Correspondingly, further research could be done on something similar.

Another important outcome comes from the combination of equations (77) with (78) and (88) or (84) with (86) and (88). The combination of equations (84), (86) and (88) is presented in Figure 30, suggesting that given the similarity of (78) to (110), the mass would typically move according to equation (78) under standard conditions. However, if the mass factors are modified, mass can move from equation (84) to equation (86), which means that mass can start traveling in the way already known but, with the appropriate values of factors, can move to equation (86) line and when to receive the required amount of energy, travel at infinite speed. In addition, even considering the movement of a mass based on (88) again, it can be concluded that, if the factors of mass are correctly selected, then mass can move to the line of equation (86) and travel with infinite speed.

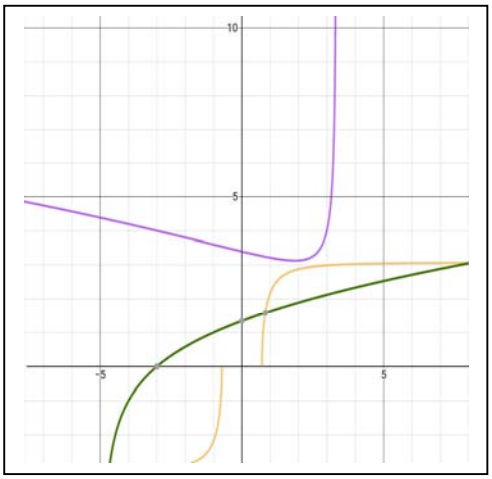

Figure 30: Graphing representation of equations (84) (green line), (86) (purple line) and (88) (yellow line)

In addition, if this combination of energy and time is inserted into equations (77) and (86), space collapses to zero. This is made apparent in the combination of Figure 1 and Figure 6, as well as Figure 13 and Figure 17. The interpretation of this combination of energy and time is that when mass receives a critical amount of energy, it can travel with infinite speed, minimizing space to zero. This condition is done at a specific value of energy which is common for speed and space, as presented in Figure 31.

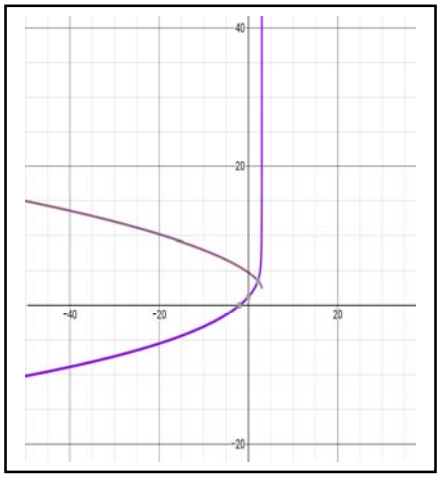

Figure 31 : Representation of equation (75) of space and (77) of speed in the same plane

4.2 Analysis of Equations Comparing to Time Parameter

The comparison of the equations (104) and (106) with equation (75) and (76) of the pem as well as the equations (108) and (109) with equations (79) and (82) of the generic model it is noticed that the results are similar in relation to time. Furthermore, the same outcome results from the comparison of the graphs that are produced from these equations. The equations (77), (78), (79) and (84) that express speed, are produced only for the equations of the expanded energy model.

This result is expected since the factors that are included in the equations derive from the equation:

$$\frac{\mathrm{E}}{\mathrm{m_0}} = \gamma c^2 \tag{122}$$

Equation (73) that expresses space can be expressed in another format, i.e.:

$$\frac{E}{m_{0T}} = \frac{{p_1}^2(2x_{i,Im}^2 - p_5)}{\cos(p_1 t + p_2)} \tag{123}$$

The implementation of equation (122) to equation (123) turns the latter to:

$$\gamma c^2 = \frac{{p_1}^2(2x_{i,Im}^2 - p_5)}{\cos(p_1 t + p_2)} \tag{124}$$

which relation indicates a relation between space and time. Similar equations can be developed for all other expressions of space. This ascertainment proves that indeed there is a relation between space and time with energy.

Graphs obtained from imaginary components of pem and generic mass equations appear as trigonometric patterns. The graphical results from equations (77) and (82) demonstrate distinct variations which stem from their differing parameters. The speed equations obtained from the imaginary components of mathematics such as equations (67) and (84) present trigonometric behavior patterns. Equation (84) produces a complex graph through its multiple discontinuities that occur within brief intervals. The sophisticated nature of the created mass structure becomes apparent through this complexity.

Three-dimensional graphs generated from equations (75), (76), (77), and (78) for pem, as well as (79), (82), (84), and (86) for generic mass, illustrate changes in space or speed as functions of two variables: energy (E) on the x-axis and time (t) on the y-axis. The 3D graphs combine elements from two-dimensional energy-time plots to display information. The graph in Figure 24 presents speed changes alongside energy and time variations where speed rises with advancing energy and time. Equation (86) becomes invalid for specific pairings between energy and time since void regions emerge in the graph.

A comparison between pairs of pem and generic mass equations shows matching characteristics in their graphs. Equations (78) and (84) show equivalent behavior patterns through their appearance of space spikes at distinctive energy-time points. Equation (86) provides more continuous spatial outputs because the formed rigid mass structure hinders quick changes during energy and time operation. The graphical data in Figures 22 and 26 demonstrates that speed improves steadily as energy and time enlarge. The system shows undefined output regions when operating at low energy alongside low time values, yet these areas display unique patterns between pem and generic mass behavior. When chosen energy-time pairs are inserted into the mathematical equations, they produce results that lead to infinite speed.

4.3 Analysis of Space Equations in Relation to Factor γ.

The comparison of equations (104) and (106) for pem, as well as (108) and (109) for the generic model, indicates a similarity with the equations (75) and (76) and also (79) and (82) that describe space with the expanded energy model. The difference between the two models is the use of the factor $r_{rel} = \gamma c^2$, which can be considered as a consequence of the equation (123).

On the other hand, the use of the γ factor, produces results that do not actually deviate from the initial relativistic expression of space. Taking as example equations (108) and (109), they can be expressed as:

$$\mathrm{x}_{i,Re}(\mathrm{t}) = \pm \mathrm{c} \sqrt{\frac{1}{\sqrt{1-\frac{u^2}{c^2}}}} \frac{\sqrt{-\cos(p_1 t + p_2) + p_3 p_1 \mathrm{e}^{p_1 \mathrm{t}} + p_4 p_1^2 \mathrm{e}^{-p_1 \mathrm{t}}}}{\sqrt{2} p_1} \tag{125}$$

and

$$x_{i,Im}(t) = \pm c \sqrt{\frac{1}{\sqrt{1-\frac{u^2}{c^2}}}} \frac{\sqrt{\cos(p_1 t + p_2) + p_5 {p_1}^2}}{\sqrt{2} p_1} \quad (126)$$

which provide expressions between space and time. These expressions are not deviating from expressions that describe the way that space changes over speed [23], [24]. The expressions are more generalised, but the format of change over the speed change is of the same type.

V. CONCLUSION

The expression of the energy obtained by a mass can be expanded if mass, either in the form of pem or in the more complicated format, is approached as a dynamic quantity. In this case space is related not only to time but energy as well, intruding a new comprehension of energy-space-time interactions. The expanded model of energy provides a wider expression of speed. The first expression approaches speed in a way that follows the limitations that are known to apply as the relativistic approach indicates. However, a different expression that arises, opens the option of mass, either in pem or complete format, to travel at speeds even higher than this of light, which is currently investigated at theoretical level, provided that the factors that express a mass are properly altered. Space, in this case, as expressed in the equations produced during the investigation, is minimized, tending to zero, as speed approaches infinite speed. What remains to be verified is the experimental and practical approach as to the speed a mass can reach, minimizing the space.

ACKNOWLEDGEMENTS

The author would like to extend his gratitude to the teams contributing to the development of ClassCalc software which has been used for the creation of the qualitative 2-dimensional graphs, the Surface Plotter 3D software which has proved invaluable in the creation of the 3-dimensional graphs and Wolfram alpha which facilitated the calculation of key parts of the derived equations.

REFERENCES

1. Tennessee Tech University https://www2.tntech.edu/leap/murdock/books/v1chap6.pdf
2. Leipzig University: https://home.uni-leipzig.de/energy/energy-fundamentals/03.htm
3. University of Notre Dame: https://www3.nd.edu/~lemmon/courses/ee224/ web-manual/ web-manual/lab1/node17.html
4. The International System of units: https://www.bipm.org/ documents/ 20126/41483022/si_brochure_8.pdf
5. The Energy Origin of Mass, George Petropoulos, Journal of Modern Physics October 2024. DOI: https://doi.org/10.4236/jmp.2024.1511077
6. Vector Derivatives, Utah University, September 7, 2015 https://www.physics.usu. edu/Wheeler/EM3600/Notes02DerivativesOfVectors.pdf
7. Vector Calculus, David Tong, University of Cambridge https://www.damtp. cam.ac.uk/user/tong/vc/vc1.pdf
8. Christopher Thomas "The Composite Function Rule (The Chain Rule)", University of Sydney 1997
9. Gilbert Strang "Derivatives by the Chain Rule", MIT Open Course Warehttps://ocw.mit.edu/courses/res-18-001-calculus-fall-2023/mitres_18_001_f17 _ch04.pdf

10. C. McMullen, Harvard University, Advanced Complex Analysis, Course Notes Math 213a, January 16, 2023 https://people.math.harvard.edu/~ctm/papers/home/text/class/harvard/213a/course/c ourse.pdf
11. Nanyang Technical University, NTU Singapore https://web.spms.ntu.edu.sg/~ydchong/ teaching/07_complex_derivatives.pdf
12. University of Minesota Twin cities https://www-users.cse.umn.edu/~garrett/m/mfms/notes_2013- 14/00_basic_complex_analysis.pdf
13. Sébastien Boisgérault, Mines ParisTech, under CC BY-NC-SA 4.0 April 25, 2017, Complex Differentiability, Universite PSL https://direns.minesparis.psl.eu/Sites/Complex-analysis/ComplexDiffere ntiability/Complex-Differentiability.pdf
14. Relativity (Kinematics) David Morin, 2007 https://bpb-us-e1.wpmucdn.com/sites.harvard.edu/dist/0/550/files/2023/11/cmchap11.pdf
15. Senior Physics Challenge 2010-Introduction to Special Relativity, J.S. Biggins, July 2, 2010 https://www.tcm.phy.cam.ac.uk/~jsb56/resources/specialrelativityhandout.pdf
16. Department of Applied Mathematics and Theoretical physics, Cambridge University https://www.damtp.cam.ac.uk/user/tong/relativity/seven.pdf
17. Introduction to Special Relativity, Andrea Latin (CERN), 7-11 October 2019, Archamps, France https://indico.cern.ch/event/817381/contributions/3412314/attachments/1835902/317 8477/Lectures.pdf
18. U.S. Particle Accelerator School, Lecture notes/Barletta,Spentzouris,Harms https://uspas.fnal.gov/materials/10MIT/Review_of_Relativity.pdf
19. The Einstein's Mass-Energy Equivalence and the Relativistic Mass and Momentum derived from the Newton's Second Law of Motion, Chinnaraji Annamalai School of Management, Indian Institute of Technology, Kharagpur, India https://www.cambridge.org/engage/apigateway/coe/assets/orp/resource/item/64815099be16ad5c57a08a11/original/theeinstein-s-mass-energy-equivalence-and-the-relativistic-mass-and-momentum-derived from-the-newton-s-second-law-of-motion.pdf
20. Special Relativity, University of Pennsylvania, Alan L. Myers https://www.seas.upenn.edu/~amyers/SpecRel.pdf
21. Introducing Special Relativity in Secondary Education, Floor Kamphorst, Utrecht, the Netherlands, 2021 https://www.fisme.science.uu.nl/publicaties/literatuur/2021_thesis_kamphorst_relativity. pdf
22. Relativity without the First Postulate, Rudolf SCHMID and Qicun SUN, Department of Mathematics, Emory University, Atlanta, Georgia 30322, USA, 2002 https://www.slac.stanford.edu/econf/C0107094/papers/Schmid577-588.pdf
23. Special Relativity, Cern, C.R. Prior https://cds.cern.ch/record/1005024/files/p1.pdf
24. The Lorentz transformation, A. Steane, Oxford University, 2010, 2011 https://users.physics. ox.ac.uk/~Steane/teaching/rel_A.pdf

Quarks and Leptons Formation by Spontaneous Fractionation of a Pair of Elementary Heavy Fermions of Cosmological Origin

Massimo Auci

ABSTRACT

This work, based on the hypothesis of the existence of a pair of heavy fermions produced by the decay of an X-boson of cosmological origin, presents a possible mechanism for the formation of ordinary matter, which is not based on symmetry-breaking fields or massive decays on high-energy scales. The model shows that, under specific conditions, the pair of heavy fermions can spontaneously fractionate into three fermion-antifermion pairs, giving rise to the observed structure of matter. Unlike models in which leptons and quarks arise through spontaneous symmetry breaking and interactions mediated by Higgs fields, this model shows that matter could originate from a quantized electromagnetic decay process based on conservation laws and topological constraints.

Keywords: bridge theory, charge fractionation, hadrons, leptons, matter-antimatter asymmetry.

Classification: LCC Code: QC793.5.F4,

Language: English

Great Britain Journals Press

LJP Copyright ID: 925682
Print ISSN: 2631-8490
Online ISSN: 2631-8504

London Journal of Research in Science: Natural & Formal

Volume 25 | Issue 8 | Compilation 1.0

Quarks and Leptons Formation by Spontaneous Fractionation of a Pair of Elementary Heavy Fermions of Cosmological Origin

Massimo Auci

ABSTRACT

This work, based on the hypothesis of the existence of a pair of heavy fermions produced by the decay of an X-boson of cosmological origin, presents a possible mechanism for the formation of ordinary matter, which is not based on symmetry-breaking fields or massive decays on high-energy scales. The model shows that, under specific conditions, the pair of heavy fermions can spontaneously fractionate into three fermion-antifermion pairs, giving rise to the observed structure of matter. Unlike models in which leptons and quarks arise through spontaneous symmetry breaking and interactions mediated by Higgs fields, this model shows that matter could originate from a quantized electromagnetic decay process based on conservation laws and topological constraints.

Keywords: bridge theory, charge fractionation, hadrons, leptons, matter-antimatter asymmetry.

Author: Department of Mathematics and Physics European International State School "Altiero Spinelli" Via Figlie dei Militari 25, 10131, Torino; Space Science Department, "Odisseo-Space" Society Via Battistotti Sassi 13, 20133, Milano, Italy.

I. GENERAL INTRODUCTION

It is usually assumed that in immediately after the Big Bang at a time $t < 10^{-43} s$, the universe was extremely curved, hot and dense [1] and when the universe cooled from $10^{-6} s$ to $10^{-4} s$, the conditions became optimal for forming the building blocks of matter, quarks and leptons. The confinement of quarks then began, which aggregated to give rise to protons and neutrons.

This scenario in no way explains how and why quarks and leptons were formed, hence why particles in nature are what they are and protons are not elementary particles as was mistakenly believed until the mid-twentieth century. Currently there are several approaches that try to justify the existence of matter as we observe it but in no case has there been an attempt to give an answer to why quarks, particles with fractional charge, exist why their origin is still a mystery [2].

In addition, the current model suggests seeking an explanation of the origin of matter using accelerators with higher and higher energies, thus experimentally finding increasingly heavy and complex particles, but preventing us from examining rare processes at medium-low energy, which could instead open new perspectives in understanding the origins of matter.

In this paper we propose a model developed using the principles of the Bridge Theory (BT) [3], [4] which is a quantum-relativistic electromagnetic theory capable of proposing a complex phenomenology that suggests the existence of a primordial generating particle, which for the moment we call X. The X-particle should have been produced in great abundance in the early stages of the creation of space-time; its creation, as the model suggests, could have induced the production of primordial hydrogen.

London Journal of Research in Science: Natural & Formal

The model that will be examined is only a first step, but it shows that the direct electromagnetic interaction that characterizes the BT, when applied to a pair of fermions produced in the decay of a primordial neutral boson, produces a spontaneous phenomenon that we call "fractionation" capable of breaking the pair of original particles into three pairs of elementary particles in two different ways. In one case, the charges of fractionated particles are compatible with those of up and down quarks, in the other with those of electrons and neutrinos, so in both cases with first-generation elementary particles. The model assigns an extremely small charge value to neutrinos, which is still unknown for the moment. The fractionation process is named X as in the case of the primordial X-particle.

II. AN INTRODUCTION TO BRIDGE THEORY

BT derives from the demonstration [5], [6] of a conjecture [7] concerning the presumed role that the transverse component of the Poynting vector of a dipole source would have in localizing energy and momentum in the form of a “quantum” formally and quantitatively in accordance with quantum theory. The quantum is formed during an interaction between two charged particles whose energy and momentum are completely transformed into the energy and momentum of an "exchange photon". This is a phenomenology described in the references [3] and [4], according to which a pair of interacting particles, regardless of their electric charge value $\pm q$, produce a Dipole electromagnetic Source (DEMS) that localises in its source zone an energy $h^* c/\lambda$ and a momentum h^*/λ in agreement with that of an exchange photon, whose wavelength λ corresponds to the minimum interaction distance achieved by the particles. The value of action associated with such a direct free electromagnetic interaction is the Planck constant $h^* = 2\pi\sigma\, q^2/c$, with $\sigma = 137.035950244954$, equal to the reciprocal value of the Sommerfeld constant. The theoretical value of the Sommerfeld’s constant was first calculated for free interactions between particles in Ref. [6], subsequently the value was revised and corrected according to the angular dimensions of the interacting charges [3], and more recently calculated in the context of the formation model of hydrogen atoms [8] and for hydrogenoid atoms with different atomic number values [9], demonstrating that the Planck action is not a true fundamental constant, because it depends on the electromagnetic coupling value α, the Sommerfeld constant, that varies, even if slightly, according to the external forces acting on the system.

Following the BT, we will show that hypothesising the existence of a X-particle energetically in balance with the DEMS produced by the interaction of a virtual pair of fermions $(Q,\bar{Q})$: $X \rightleftarrows Q\bar{Q}$, if the pair have an unit of charge equal to that of the proton $\left(Crg(Q) = e^{\dagger}, Crg(\bar{Q}) = -e^{\dagger}\right)$, the cross on the charge distinguishes the charge of the proton from that of the electron without cross, provided that the two particles have sufficient interaction energy to give rise a pair proton-antiproton $E > 2m_p c^2$, the pair $(Q,\bar{Q})$ undergoes a spontaneous fractionation following two equiprobable channels giving rise to two distinct groups of three pairs of elementary particles.

The first group consists of three pairs of particles with fractional charges in the quark-antiquark form $Q\bar{Q} \rightarrow d\bar{d} + 2u\bar{u}$, the second group consists in three pairs of leptons, one pair electron-positron and two pairs of electronic neutrino-antineutrino in the form $Q\bar{Q} \rightarrow e\bar{e} + 2\nu\bar{\nu}$.

Since in this model neutrinos are expected to have an extremely weak but not zero fractionary electric charge, because they must be able to interact electromagnetically even if weakly with other matter, the electron and positron consequently have a lower charge value than that of the proton unit.

III. STRUCTURE FUNCTION OF TWO INTERACTING CHARGE FRAGMENT

Starting from the principle of BT that all DEMS formed by the interaction of a pair of elementary particles are associated with a value of action expressed in Dirac form, one formally describes the process that gives rise to the action in a DEMS formed by the particles (a,b) with an Abelian operator $a \odot b$ that returns the value of action of their interaction.

Considering the virtual interacting pair $(Q,\bar{Q})$ forming a DEMS with the same mass energy of the X-particle, one assumes that when the two particles interact, an expanding electromagnetic bubble delimited by the emitted spherical wave of wavelength λ is formed.

Inside the bubble, a spontaneous fragmentation of the original pair $(Q,\bar{Q})$ occurs, breaking the primitive DEMS into three sub-DEMS, each produced by the interaction of a pair of particles $(x_i,\bar{x}_i)$, with fractionary charges $Crg(x_i)=\chi_i e^{\dagger}$ and $Crg(\bar{x}_i)=\bar{\chi}_i e^{\dagger}$, where $0<\chi_i<1$, $\bar{\chi}_i=-\chi_i$ with $i=1,2,3$ are the fractionary dimensionless charges such a that

$$\begin{aligned} Crg(Q) &= \sum_i Crg(x_i) = +e^{\dagger} \\ Crg(\bar{Q}) &= \sum_i Crg(\bar{x}_i) = -e^{\dagger} \end{aligned} \tag{1}$$

In general, taken two particles (x_i,x_j), the corresponding action is given by

$$\hbar_{ij} = x_i \odot x_j \equiv \sigma_{\chi_i\chi_j}\frac{e^2}{c} \tag{2}$$

with c speed of light and $\sigma_{\chi_i\chi_j}$ electromagnetic structure constant of the action, corresponding to the reciprocal value of the coupling constant between particle and field $\alpha_{ij}=\sigma^{-1}_{\chi_i\chi_j}$, calculated by the expression

$$\sigma_{\chi_i\chi_j} = \left(\frac{4\pi}{3}\int_0^{\pi}\Theta_t(\chi_i,\chi_j,\rho,\theta)d\theta \; - \frac{\chi_i\chi_j}{4\pi\rho^2}\right) \tag{3}$$

in which the function

$$\begin{aligned} \Theta_t(\chi_i,\chi_j,\rho,\theta) = 16 & \sqrt{\frac{\chi_i^2}{\left(4+\rho^2+4\rho\cos\theta\right)^2}+\frac{\chi_j^2}{\left(4+\rho^2-4\rho\cos\theta\right)^2}+\frac{2\chi_i\chi_j\left(4-\rho^2\right)}{\sqrt{\left[\left(4+\rho^2\right)^2-16\rho^2\cos^2\theta\right]^3}}} \\ & \cdot\left|\frac{\chi_i\left(2+\rho\cos\theta\right)}{\sqrt{\left(4+\rho^2+4\rho\cos\theta\right)^3}}+\frac{\chi_j\left(2-\rho\cos\theta\right)}{\sqrt{\left(4+\rho^2-4\rho\cos\theta\right)^3}}\right| \end{aligned} \tag{4}$$

is the field structure of the transversal component of the Poynting vector of the electromagnetic field of the DEMS produced by the two interacting particles (Cf. Ref. [9]).

Using Eq. (2) for pair of particles $(x_i,\bar{x}_i)$, from Eq. (3a) and (3b) it appears that the action associated with the interactions between:

- *proton - antiproton* $$\hbar^{\dagger} = p \odot \overline{p} \equiv \sigma \frac{e^{\dagger 2}}{c} \tag{5}$$

- *electron – positron* $$\hbar = e \odot \overline{e} \equiv \sigma \frac{e^{2}}{c} \tag{6}$$

is in both cases the same, because the structure constant σ associated to pairs of particles is independent of their electric charge. Equation (3a) can be represented as a function of the ratio $\rho = R/\lambda$ between the dipole moment length per unit of charge R and the wavelength λ of the DEMS.

Therefore, using the Eq. (2), the value of the action calculated in Gauss units for an interaction between a pair $\left(Q,\overline{Q}\right)$ during the fractionation is given by

$$Q \odot \overline{Q} = \sum_i x_i \odot \overline{x}_i = \frac{e^{\dagger 2}}{c} \sum_i \sigma_{\overline{\chi}_i \chi_i} \tag{7}$$

with

$$\sigma_{\chi_i \overline{\chi}_i} = \sigma \chi_i^2 \tag{8}$$

From Eq. (5), (6) and (7) it results

$$1 = \sum_i \chi_i^2 \tag{9}$$

For a free electromagnetic interaction between a pair of charged particles, i.e., without external constraints acting on the DEMS, the ratio was been calculated numerically using a stochastic method described in Ref. [3] and [7] and its value it is known exactly $\rho^{*} = 1.275556618599942$. Using this ratio the value of the structure constant is $\sigma^{*} = 137.035989$. Each external constraint acting on the pair during their direct interaction produces a variation of the value of the ratio ρ and consequently of the structure constant as proven in Ref. [8] for the electron-proton capture and [9] for the interaction of the orbital electrons with the atomic nucleus.

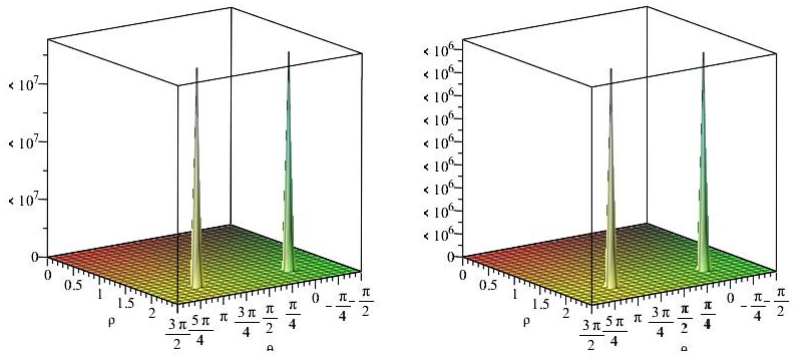

(a) (b)

Figure 1

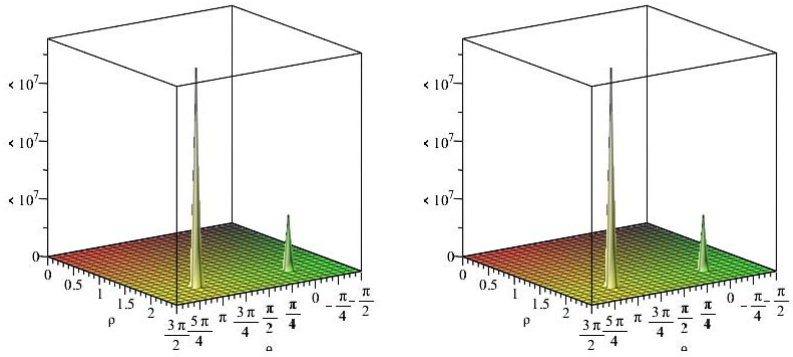

(c) (d)

Figure 1: field structure (4) of the transversal component of the Poynting vector. (a) for the direct interaction of pairs $u\bar{u}$; (b) for the direct interaction of pairs $d\bar{d}$; (c) for the direct interaction of $u\bar{d}$; (d) for the direct interaction of ud. In letters (c) and (d) there are differences that are not graphically appreciated.

IV. FRACTIONATION OF THE UNIT PROTON CHARGES: SOLUTIONS L AND H TO BUILD THE PARTICLES OF THE UNIVERSE

When two charged particles interact freely, the DEMS produced continues to exist regardless of the distance achieved by the two moving away particles. The DEMS produced, by means of the specific value of action that must remain constant over time, entangles the two particles inside of the electromagnetic spherical bubble bounded by the emitted wavefront, so that any action suffered by each of the two particles, produces a coordinate and instantaneous variation on the other particle as well (See Ref. [4]).

For a DEMS produced by two virtual interacting particles $(Q,\bar{Q})$ the action must be conserved, therefore, the following basic principles apply:

A. The total action $Q \odot \bar{Q}$ is a constant value of the DEMS. Considering a fractionation of the pair of particle $(Q,\bar{Q})$ in three sub-DEMS with a small loss of action provided that the total energy of the system remains unchanged, using equations (9) the total action of the three cells must not exceed in value the total action of the primary bubble.

$$\sum_i \chi_i^{\,2} \le 1. \tag{10}$$

B. The total charge is conserved. The total fractional charge must be equal to that original:

$$\sum_i \chi_i = \pm 1\,. \tag{11}$$

C. In nature protons are primordial particles formed by three quarks of which two quarks have the same value of fractionary charge. Considering this abundance, two of the three charge fragments obtained must have equal value of charge:

$$\chi_2 = \chi_3. \tag{12}$$

The three previous conditions (A-B-C) are summarized by the systems:

$$\begin{cases} \bar{\chi}_1^2 + \bar{\chi}_2^2 + \bar{\chi}_3^2 \leq 1 \\ \bar{\chi}_1 + \bar{\chi}_2 + \bar{\chi}_3 = -1 \\ \bar{\chi}_2 - \bar{\chi}_3 = 0 \end{cases} \quad \begin{cases} \chi_1^2 + \chi_2^2 + \chi_3^2 \leq 1 \\ \chi_1 + \chi_2 + \chi_3 = +1 \\ \chi_2 - \chi_3 = 0 \end{cases} \tag{13a}$$

The equations (13a) can be transformed in the form

$$\begin{cases} \bar{\chi}_1 = -1 - 2\bar{\chi}_3 \\ \bar{\chi}_2 = \bar{\chi}_3 \\ (3\bar{\chi}_3 + 2)\bar{\chi}_3 \leq 0 \end{cases} \quad \begin{cases} \chi_1 = +1 - 2\chi_3 \\ \chi_2 = \chi_3 \\ (3\chi_3 - 2)\chi_3 \leq 0 \end{cases} \tag{13b}$$

The third inequation of the first system (13b) has solutions in the interval $\bar{S} = \left\{ \bar{\chi}_3 \in \left[-\frac{2}{3} \quad 0 \right] \right\} \cap \mathbb{R}^-$ for a negative charge generator and in the interval $S = \left\{ \chi_3 \in \left[0 \quad +\frac{2}{3} \right] \right\} \cap \mathbb{R}^+$ for a positive charge generator and solutions respectively $\bar{S}_0 = \left\{ -\frac{2}{3}, 0 \right\}$ and $S_0 = \left\{ 0, +\frac{2}{3} \right\}$ for the corresponding associated equations. Therefore, considering that in the act of fractionation a small but finite amount of action is lost through a variation in the charge values of the fragments, but not in the energy that is conserved, we can write the solution for a negative generator as $\bar{S} = \left\{ \bar{\chi}_3 \in \left[\lim_{\varepsilon_Q \to \delta c} \left(-\frac{2}{3} + \varepsilon_Q \right) \quad \lim_{\varepsilon_Q \to \delta c} \left(0 - \varepsilon_Q \right) \right] \right\} = \left\{ \bar{\chi}_3 \in \left[-\frac{2}{3}^{(+)} \quad 0^{(-)} \right] \right\}$;

analogously for a positive generator $S = \left\{ \chi_3 \in \left[\lim_{\varepsilon_Q \to \delta c} \left(0 + \varepsilon_Q \right) \quad \lim_{\varepsilon_Q \to \delta c} \left(+\frac{2}{3} - \varepsilon_Q \right) \right] \right\} = \left\{ \chi_3 \in \left[0^{(+)} \quad +\frac{2}{3}^{(-)} \right] \right\}$ with in both cases $0 < \delta c < \varepsilon_Q$ where δc is a tiny non-zero charge constant for each pair of solutions $(\bar{S}, S)$. Considering that among all the infinite particular solutions inside the intervals $\bar{S}$ and S, the values $\bar{\chi}_3$ and χ_3 must be those that minimize the difference of action between the initial action and the final total action satisfying the Eq. (10), only the extremes of the intervals $\bar{S}$ and S satisfy exactly these conditions, therefore, the final solutions can be written in the form $\bar{\chi}_3 = \left(-\frac{2}{3}^{(+)}, 0^{(-)} \right)$ for the negative generator and $\chi_3 = \left(+\frac{2}{3}^{(-)}, 0^{(+)} \right)$ for the positive generator. The superscriptions $(-)$ or $(+)$ at right of the values of charge with theirs eventual multiplicity expresses the charge tendency (CT) defined as a scalar dimensionless multiple δc, which is the defect or excess of electric charge respectively to the solutions $(\bar{S}_0, S_0)$ obtained in Eq. (13b) using instead of inequalities their associated equations. The CT at the moment does not define an exact value of the charge.

Using the two pairs of generators and the first two equations of the Eq. (13b), one obtains the complete sets of the charge fractionated divided into anticharge and charge for hadronic (*H*) and leptonic (*L*) type

$$\bar{\chi}_3 = \left(-\frac{2}{3}^{(+)} \;,\; 0^{(-)} \right) \rightarrow \begin{cases} \bar{H} = \left(+\frac{1}{3}^{(--)} \quad -\frac{2}{3}^{(+)} \quad -\frac{2}{3}^{(+)} \right) \\ \bar{L} = \left(-1^{(++)} \quad 0^{(-)} \quad 0^{(-)} \right) \end{cases}$$

$$\chi_3 = \left(+\frac{2}{3}^{(-)} \;,\; 0^{(+)} \right) \rightarrow \begin{cases} H = \left(-\frac{1}{3}^{(++)} \quad +\frac{2}{3}^{(-)} \quad +\frac{2}{3}^{(-)} \right) \\ L = \left(+1^{(--)} \quad 0^{(+)} \quad 0^{(+)} \right) \end{cases} \tag{14}$$

by demonstrating how the solutions obtained for the systems in Ec. (13) are unique and depend on charge and action conservation.

To analyse the meaning of the solutions achieved in Eq. (13), one defines as hadronic the solutions in which we have three fractional values of the generator in agreement with the existence of two flavours of quarks

$$\mathbf{H} = \begin{pmatrix} H \\ \bar{H} \end{pmatrix} = \begin{pmatrix} -\frac{1}{3}^{(++)} & +\frac{2}{3}^{(-)} & +\frac{2}{3}^{(-)} \\ +\frac{1}{3}^{(--)} & -\frac{2}{3}^{(+)} & -\frac{2}{3}^{(+)} \end{pmatrix} \Leftrightarrow \begin{pmatrix} d & u & u \\ \bar{d} & \bar{u} & \bar{u} \end{pmatrix}, \tag{15a}$$

and leptonic the solutions

$$\mathbf{L} = \begin{pmatrix} L \\ \bar{L} \end{pmatrix} = \begin{pmatrix} +1^{(--)} & 0^{(+)} & 0^{(+)} \\ -1^{(++)} & 0^{(-)} & 0^{(-)} \end{pmatrix} \Leftrightarrow \begin{pmatrix} \bar{e} & \nu & \nu \\ e & \bar{\nu} & \bar{\nu} \end{pmatrix} \tag{15b}$$

where all particles in addition to the declared charge value have a CT, i.e. the charges are not exactly equal to the usual declared values. Considering that the CT changes in signs if the sign of the unitary generator changes, CT allows all the cells to get a part of the total energy of the primordial DEMS allowing them to evolve energetically. It is important to highlight that in this model all neutral interactions must have total zero tendency to conserve the total charge, in general the sum of the CT of the particles involved in the reaction channel must have the same tendency before and after the reaction.

For the solutions (15a) and (15b) the immediate consequence is that the proton must have a value of charge an amount $2\delta c$ greater than the unit charge of the positron, for coherence $e^{\dagger} > e$ by reopening a discussion on the real neutrality of atoms and molecules [10], [11]. This allows us to suppose that the true unit of charge is that of the proton and not that of the electron, although experimentally difficult to distinguish from that of the proton, because it is obtained by fractionation from that of the proton.

To describe hadrons in Eq. (15a), the CT is not an essential formalism because hadrons, unlike neutrinos, have enough charge to interact with each other and the CT could only be significant by studying the behaviour during interactions between non-elementary particles, a study that is beyond the scope of this article. In this context, it is sufficient to know that there exists a fractionation mechanism that leads hadron charges not to have the declared charge value but to have marked positive or negative tendencies that can affect their way of interacting. In fact, the CT could be responsible to define the colour charge of quarks, allowing a direct interaction between quarks of the same type, an example for stable particles could be the proton $Crg(p) = \left(+\frac{2}{3}^{(-)} \; +\frac{2}{3}^{(--)} \; -\frac{1}{3}^{(+++)} \right)$.

The three charges can be considered equivalent to that u-RED, u-GREEN and d-BLUE, where the CT sign is chosen in such a way that the resulting proton uud formed by the three quarks taken together can form a particle of exact unit charge with zero tendency in accordance with QCD and with a charge only slightly greater than that of the electron.

Since the use of the CT notation for the hadronic solution currently appears redundant, we will use it only when and if necessary.

Spontaneous Fractionation
of a Neutral Boson into Fermionic Matter via DEMS State

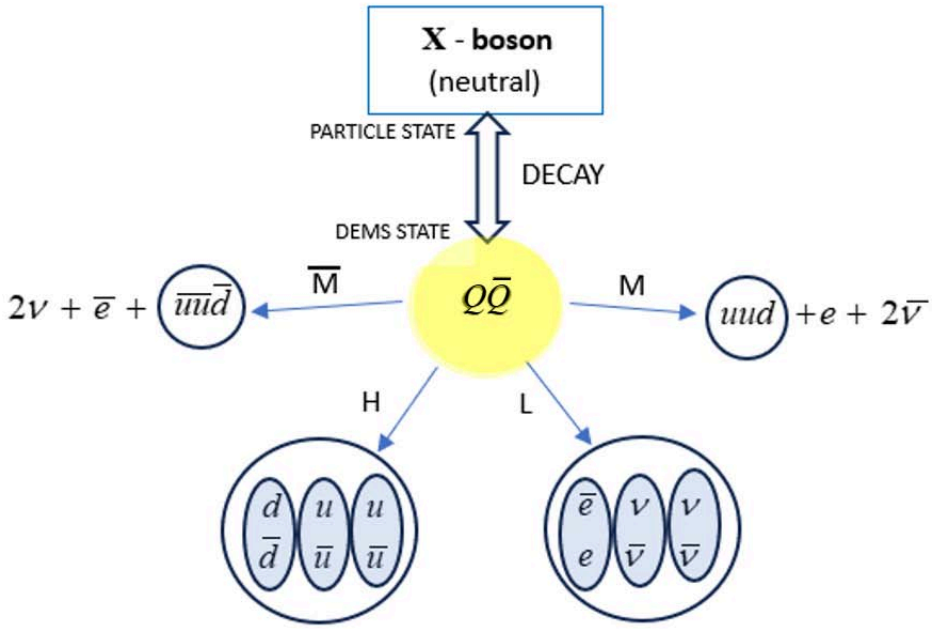

Figure 2: This schematic visually emphasizes the transition from the heavy neutral X-boson to the fermion structure of matter via spontaneous, quantized charge fractionation: (M) matter in hydrogen form; $(\bar{M})$ antimatter in antihydrogen form; (H) hadronic configuration; (L) lepton configuration.

V. MIXED SOLUTIONS: DIRECT ATOMS FORMATION

The solutions of the systems in Eq. (13a) provides for two fundamental charging solutions χ_3. In Eq. (14) the final solutions obtained by assigning corresponding values to χ_3 and to $\bar{\chi}_3$ have been considered, thus assigning the same type of solution. For example, $\chi_3 = +2/3$ and $\bar{\chi}_3 = -2/3$, obtaining for the other two solutions respectively ($\chi_2 = +2/3$, $\chi_1 = -1/3$) and ($\bar{\chi}_2 = -2/3$, $\bar{\chi}_1 = +1/3$). In this way, the two original particles $(Q,\bar{Q})$ are fractionated into three pairs of elementary particles, exactly as in reality where the particles are created in pairs (See Eq. (15a) and (15b) in the previous paragraph).

However, there is no obvious reason not to consider mixed solutions within the DEMS itself. Thus, a Q particle can be fractionated hadronically and a $\bar{Q}$ particle in a lepton way or vice versa. This possibility would lead to the formation of the mixed matrices:

$$\mathbf{M}=\begin{pmatrix} H \\ \bar{L} \end{pmatrix}=\begin{pmatrix} -\frac{1}{3} & +\frac{2}{3} & +\frac{2}{3} \\ -1^{(++)} & 0^{(-)} & 0^{(-)} \end{pmatrix}\Leftrightarrow\begin{pmatrix} d & u & u \\ e & \bar{\nu} & \bar{\nu} \end{pmatrix} \tag{16}$$

and its symmetric

$$\bar{\mathbf{M}}=\begin{pmatrix} \bar{H} \\ L \end{pmatrix}=\begin{pmatrix} +1^{(--)} & 0^{(+)} & 0^{(+)} \\ +\frac{1}{3} & -\frac{2}{3} & -\frac{2}{3} \end{pmatrix}\Leftrightarrow\begin{pmatrix} \bar{e} & \nu & \nu \\ \bar{d} & \bar{u} & \bar{u} \end{pmatrix} \tag{17}$$

obtained with a mixing of compatible solutions H and L. The choice of which of the two matrices is the anti-matrix is arbitrary, in this context the one containing the elementary particles of ordinary matter compatible with the existence of hydrogen atoms has been chosen as the matrix and the one containing the particles compatible with the existence of antihydrogen atoms has been chosen as the anti-matrix.

In this case one could have the coexistence in a same electromagnetic bubble of the constituents of a proton or antiproton and of three leptons violating the principle of creation in pairs of the particles associated to the sub-DEMS.

This may be possible if the fractionation occurs by single particles and not by pairs, in this case the mixed bubble does not violate the invariance of the total charge, of the spin of the bubble and does not violate the invariance of the sum of the baryon and lepton numbers

$$B+L=0 \tag{18}$$

but it would seem to violate the action conservation principle (A), in fact, Eq. (7) shows that the fractionation process is completely invariant in the action only if it occurs in pairs. On the other hand, the inequality of equation (10) confirms that a small part of the action is lost due to the fractionation for the appearance of the CT, which also happens if the fractionation occurs not in pairs but in single particles, exactly as in the asymmetric fractionation characterized by the mixed solutions (16) and (17) which is invariant-action only if the interaction occurs between groups of particles, with each group formed in such a way as to have a total unitary charge. In this case, one supposes that the charges of the quarks remaining confined together and interacting among them, can produce a proton. The electron remains alone because the two low-charged neutrinos have the possibility of escaping by subtracting a lot of energy from the lepton group, thus making it more likely that it will be captured by the proton and the formation of a hydrogen atom [9].

This process suggests that if one collects all solutions with the different charged particles in the X-matrix below

$$\mathbf{X}=\begin{pmatrix} -1^{(++)} & 0^{(-)} & 0^{(-)} \\ +1^{(--)} & 0^{(+)} & 0^{(+)} \\ -\frac{1}{3} & +\frac{2}{3} & +\frac{2}{3} \\ +\frac{1}{3} & -\frac{2}{3} & -\frac{2}{3} \end{pmatrix}\Leftrightarrow\begin{pmatrix} e & \bar{\nu} & \bar{\nu} \\ \bar{e} & \nu & \nu \\ d & u & u \\ \bar{d} & \bar{u} & \bar{u} \end{pmatrix} \tag{19}$$

Considering the presence in spacetime of a sufficient number of particles produced by the X process, it is possible to obtain invariant DEMS in action, formed by two groups of particles in direct interaction, each with a total integer charge. The groups are obtained by aggregating the different elementary particles available in the X matrix in a different way. Each group corresponds to a possible non-elementary particle.

Extending these considerations, charge groups can be produced using the elementary particles in the matrix (19) in such a way that the initial charge values can be reproduced forming new particles as for example $p \equiv uud$, $\bar{p} \equiv \bar{u}\bar{u}\bar{d}$ or $\pi^+ \equiv u\bar{d}$, $\pi^- \equiv \bar{u}d$, $\Delta^- = ddd$, $\Delta^+ = \bar{d}\bar{d}\bar{d}$ and so on, but there is also the possibility of produce heavy groups with fractional charges of successive generation as $\bar{d}^{(II)} = d\bar{d}\bar{d}$, $\bar{d}^{(III)} = u\bar{u}\bar{d}$ and $d^{(II)} = d\bar{d}d$, $d^{(III)} = u\bar{u}d$ or $\bar{u}^{(II)} = d\bar{d}\bar{u}$, $\bar{u}^{(III)} = u\bar{u}\bar{u}$ and $u^{(II)} = d\bar{d}u$, $u^{(III)} = u\bar{u}u$ or particles with charge greater than one as $\Delta^{++} = uuu$. These are just some of the possible groups and others, all in accordance with the symmetry of the Standard Model are possible and can be connected to quarks belonging to the second and third generations or later. In this sense, it is possible that the generations following the third differ from the previous generations only in the energy content, but if the energy required to operate the DEMS exceeds the mass energy of the primordial neutral boson X, the generations following the third will not be possible.

This model is the only one that can be used to maintain unchanged the charge and action during the formation of a DEMS between two charge groups.

The X-matrix (19) puts in evidence a perfect symmetry in particles-antiparticles primary production with an abundance of two neutrinos for each hydrogen atom and two antineutrinos for each antihydrogen atom, having four neutrinos for each pair of hydrogen-antihydrogen. Considering that at the current stage it is not yet possible to know where and when anti-hydrogen disappears, starting from Eq. (19) could be interesting in the future to try to draw all possible scenarios able to describe the universe.

IV. DISCUSSION AND CONCLUSIONS

Considering that by using the Eq. (7) and (8), the quantum energy of a DEMS produced by the interaction of two proton unit charge is given by $E = \sigma e^{\dagger 2}/\lambda$ and that the value of the Planck action $\sigma e^{\dagger 2}/c$ depends by the value of the dipole ratio $\rho = R/\lambda$ and by the value of the square of the interacting unit charge, exist two possibility to modify the value of the quantum energy of the DEMS: modify the dipole ratio acting on the dipole length R or on the wavelength λ; modify the value of the square of the unit charge $e^{\dagger 2}$ involved in the interaction. The former, modify the structure function of the DEMS but can be produced only under the action of external constraints, the last, since the fractionating is a spontaneous internal process, occurs under the action of internal constraints that not modify the structure constant but only the charge distribution of the fragments, reducing the total action involved. In fact, Eq. (9) is verified for an exact fractionation in which the charge tendency δc is equal to zero, but assuming a non-zero charge tendency $\delta c \neq 0$, only Eq. (10) with a strict inequality can be verified, while preserving the total charge of the system. Therefore, considering a tendency value of the charge at the limits of experimental measurability, the reduction of the action value produced by Eq. (10), although instrumentally imperceptible, reduces the total action and energy value of DEMS. However, since the energy must be conserved, the wavelength will undergo a shift towards blue such as to keep the final energy unchanged, also raising the action value, at the expense of the structural constant. In fact, the charging tendency value is expected to be extremely small. This agrees with the possible presence of a charge value associated with neutrinos, without which in BT they could not gain mass. An experimental way to determine the CT is to measure the neutrality of the hydrogen,

because the charge of an electron is $Crg(e) = -e^{\dagger} + 2\delta c$ and then, that of a proton $Crg(p) = e^{\dagger}$, in such a way that $\delta c = \frac{Crg(e) + Crg(p)}{2}$.

The mechanism of spontaneous fractionation presented demonstrates a new framework for the generation of fermionic matter based exclusively on the properties of the electromagnetic field. Unlike conventional models rooted in symmetry breaking dynamics and massive decay of the gauge boson, this model proposes an intrinsic structure of matter formation that emerges from fundamental constraints of charge and action. This provides a basis for reasoning within new scenarios about hydrogen dominance and the presence of three generations of fermions, using only electromagnetic interaction. However, the identification of the X particle, i.e. the boson that has the expected role of generating hadrons and leptons, in the early universe and in the experimental reality of accelerator physics, will be fundamental.

In fact, the model developed is able to justify the existence in the universe of four different fermions (u,d,e,ν) and four different antifermions $(\bar{u},\bar{d},\bar{e},\bar{\nu})$, each associated with a fractional charge and with properties similar to those experimentally known in nature and predicted by the Standard Model. Excluding the value of the mass of the electron, which is well known, it could be interesting to estimate in a consistent way the masses of quarks and neutrinos, but at the current stage of development of the research work, the results are not yet obtainable from the model.

As seen above, the introduction of the CT allows us to suggest a mechanism that justifies the existence of the colour charge of quarks, giving in this case the possibility to two apparently identical particles to interact electromagnetically by binding to each other. Unfortunately, exact calculations can only be developed after an estimate of the charging trend value.

Finally, it may be interesting to consider that following the model, matter and antimatter would have as a distinctive characteristic the sign of the charge generator, when the sign is positive the fractionation produces particles, when the sign is negative the fractionation produces antiparticles. So the electron would be the antiparticle of the positron, this for a hydrogen-filled universe means that there are as many protons as electrons, so since the proton is made up of three quarks uud defined all as particles and one electron defined as antiparticle, defining a number of asymmetry matter-antimatter $M = \pm 1$, a hydrogen atom would be formed by a particle (proton) with $M = 1$ and an antiparticle (electron) with $M = -1$, unless the negligible presence of neutrinos and antineutrinos in pairs, this would solve the problem of matter-antimatter asymmetry in the universe in terms of particles-antiparticles asymmetry, in fact, hydrogen would consist of a particle and an antiparticle with an asymmetry $M = 0$ resolving in conceptual terms the apparent asymmetry matter-antimatter in favours of matter in the universe.

The fact that the matter-antimatter asymmetry can be considered equal to zero, however, does not solve the problem of the absence of antihydrogen in the early universe. However, the author believes that the identification of a candidate particle to be the X-boson would allow to obtain a scale factor capable of assigning a mass to quarks and neutrinos, helping to find a way to understand the baryon asymmetry of the universe.

Funding Statement: This study is not supported by grants.

Conflict of Interest declaration: The author declare that they have no affiliations with or involvement in any organization or entity with any financial interest in the subject matter or materials discussed in this manuscript.

Ethical Conduct: In these studies, no procedures involved human participants.

Data Availability Statements: The presented article is not associated with any experimental data nor with theoretical data calculated using models. All necessary data is present in the text or associated references.

REFERENCES

1. J. Rafelsky. "Quarks in the Universe". Int. Journal of Modern Phys. E. 16, 03, 813-828 (2007). https://doi.org/10.1142/S0218301307006307
2. Di Bari, P. (2022) On the Origin of Matter in the Universe. *Progress in Particle and Nuclear Physics*, 122, Article ID:103913. https://doi.org/10.1016/j.ppnp.2021.103913
3. M. Auci, G. Dematteis. "An approach to unifying classical and quantum Electrodynamics". Int. Journal of Modern Phys D. B13, 1525 (1999). https://doi.org/10.1142/S0217979299001569
4. M. Auci. "Superluminality and Entanglement in an Electromagnetic Quantum-Relativistic Theory". Journal of Modern Physics, 9, 2206-2222 (2018). https://doi.org/10.4236/jmp.2018.912139
5. M. Auci. "A conjecture on the physical meaning of the transversal component of the Poynting vector. II. Bounds of a source zone and formal equivalence between the local energy and the photon." Phys. Lett. A 148, 399 (1990). https://doi.org/10.1016/0375-9601(90)90488-A
6. M. Auci. "A conjecture on the physical meaning of the transversal component of the Poynting vector. III. Conjecture, proof and physical nature of the fine structure constant". Phys. Lett. A 150, 143 (1990). https://doi.org/10.1016/0375-9601(90)90109-2
7. M. Auci. "A conjecture on the physical meaning of the transversal component of the pointing vector". Phys. Lett. A 135, 86 (1989). http://doi.org/10.1016/0375-9601(89)90650-6
8. M. Auci. "Estimation of an absolute theoretical value of the Sommerfeld's fine structure constant in the electron–proton capture process". Eur. Phys. J. D 75, 253 (2021). https://doi.org/10.1140/epjd/s10053-021-00253-x.
9. M. Auci. "On a Non-Standard Atomic Model Developed in the Context of Bridge Electromagnetic Theory". J. of Phys. - Chem. & Biophysics Vol 14, 5. (2024). https://doi.org/10.35 841/2161- 0398.24. 14.401
10. S. Batkin and M. K. Sundaresan. "*A new method to improve the limit on the electric charge of the neutrino*". J. Phys. G: Nucl. Part. Phys. 20 1749 (1994).https://doi.org/10.1088/0954-3899/20/11/004
11. Jens C. Zorn, George E. Chamberlain, and Vernon W. Hughes. "Experimental Limits for the Electron-Proton Charge Difference and for the Charge of the Neutron". Phys. Rev. 129, 2566 (1963). https://doi.org/10.1103/PhysRev.129.2566

Synthesis and *in Silico* Biological Activity of Novel Bridged Systems based on 5-Formyl Derivatives of Pyrimidine-4,6-Diols

Aleksandr V. Dambaev, Denis A. Kolesnik, Igor P. Yakovlev, Marina V. Sopova, Gleb V. Kondratyev & Polina O. Levshukova

ABSTRACT

The growing body of publications on the synthesis of 1,3-diazine-bridged systems has drawn increasing attention to these compounds. The aim of our work was to synthesise novel bisazomethines derived from 4,6-dihydroxy-2-methylpyrimidine-5-carbaldehyde (**1**). A series of Schiff bases was obtained via nucleophilic addition of aliphatic diamines to the carbonyl group of substrate **1**. Water was employed as the sole solvent during synthesis, affording target products in 85–90% isolated yields. Structural confirmation was achieved by ^{1}H and ^{13}C nuclear magnetic resonance (NMR) spectroscopy. In silico screening (PASS Online, CLC-pred, Antivir-pred, and GUSAR Online) revealed that the synthesised bisazomethines exhibit broad-spectrum bioactivity, including antihypertensive, antibacterial, and anticancer properties, while maintaining Class 4 toxicity (low risk). Thus, we report novel bridged bisazomethines based on a 5-formyl derivative of 2-methylpyrimidine-4,6-diol, which combine a promising safety profile with multifaceted biological activity.

Keywords: 4,6-dihydroxypyrimidine- 5-carbaldehyde, nucleophilic addition, schiff bases, bisazomethines.

Classification: LCC Code: QD401

Language: English

Great Britain Journals Press

LJP Copyright ID: 925683
Print ISSN: 2631-8490
Online ISSN: 2631-8504

London Journal of Research in Science: Natural & Formal

Volume 25 | Issue 8 | Compilation 1.0

Synthesis and *in Silico* Biological Activity of Novel Bridged Systems based on 5-Formyl Derivatives of Pyrimidine-4,6-Diols

Aleksandr V. Dambaev[α], Denis A. Kolesnik[σ], Igor P. Yakovlev[ρ], Marina V. Sopova[CD], Gleb V. Kondratyev[§] & Polina O. Levshukova[χ]

ABSTRACT

The growing body of publications on the synthesis of 1,3-diazine-bridged systems has drawn increasing attention to these compounds. The aim of our work was to synthesise novel bisazomethines derived from 4,6-dihydroxy-2-methylpyrimidine-5-carbaldehyde (1). A series of Schiff bases was obtained via nucleophilic addition of aliphatic diamines to the carbonyl group of substrate 1. Water was employed as the sole solvent during synthesis, affording target products in 85–90% isolated yields. Structural confirmation was achieved by ^{1}H and ^{13}C nuclear magnetic resonance (NMR) spectroscopy. In silico screening (PASS Online, CLC-pred, Antivir-pred, and GUSAR Online) revealed that the synthesised bisazomethines exhibit broad-spectrum bioactivity, including antihypertensive, antibacterial, and anticancer properties, while maintaining Class 4 toxicity (low risk). Thus, we report novel bridged bisazomethines based on a 5-formyl derivative of 2-methylpyrimidine-4,6-diol, which combine a promising safety profile with multifaceted biological activity.

Keywords: 4,6-dihydroxypyrimidine- 5-carbaldehyde, nucleophilic addition, schiff bases, bisazomethines.

I. INTRODUCTION

Nitrogen-containing heterocyclic systems are among the most significant structures used in the synthesis of active pharmaceutical ingredients. Classically, compounds containing 1,3-diazine cycle are used in the therapy of oncological, cardiovascular and infectious diseases [1]. Active pharmaceutical substances such as imatinib, bosentan, trimethoprim, voriconazole and many others owe their pharmacological action also to the pyrimidine moiety (Fig. 1). It is pertinent to note that compounds containing azomethine groups exhibit a broad spectrum of biological activity, including antibacterial, antidepressant, and neuroprotective properties [2,3]. Importantly, metal-organic complexes derived from pyrimidine-based bisazomethines demonstrate significant promise as antibacterial and antifungal agents [4,5]. However, as is well documented, microbial resistance to antimicrobial agents continues to rise inexorably, while oncological and cardiovascular diseases remain unconquered. This is what makes it necessary to continuously search for new biologically active molecules potentially capable of prolonging human life and improving its quality. The aim of our study was to synthesise novel bisazomethines derived from 4,6-dihydroxy-2-methylpyrimidine-5-carbaldehyde, which preliminary in silico screening suggests may exhibit antihypertensive, antibacterial, and antitumour activities. In this work, we developed a laboratory-scale synthetic route to both 5,5'-{1,2-ethylenebis [azanylylenem ethylidenyl]}bis(2-methylpyrimidine-4,6-diol) and 5,5'-{propane-1,2-diylbis [azaniliden emeth ylidenyl]}bis(2-methylpyrimidine-4,6-diol) with high isolated yields (80% and 90%, respectively).

London Journal of Research in Science: Natural & Formal

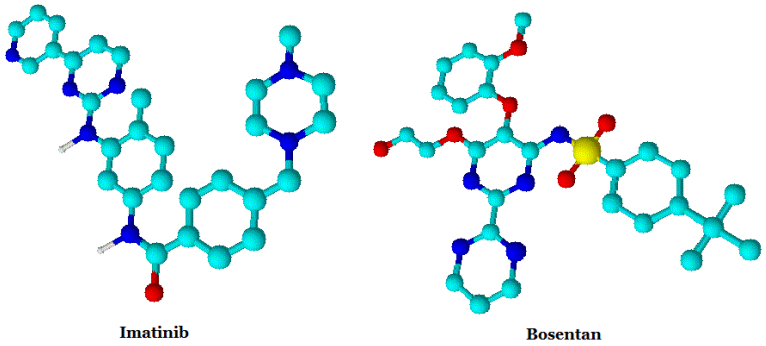

Figure 1: Structural formulas of imatinib and bosentan

II. MATERIAL AND METHODS

Preliminary screening of biological activity was performed using specialised web resources. PASS-online [6] was used as the most extensive database in terms of the number of putative activities, CLC-pred was used to analyse the possibility of antitumour activity, and Antivir-pred was necessary to study the obtained structures for antiviral activity. The estimated acute toxicity profile was assessed using the GUSAR-online web resource.

The carbonyl component used was 4,6-dihydroxy-2-methylpyrimidine-5-carbaldehyde (1), which was prepared according to previously developed method by the interaction of 2-methylpyrimidin-4,6-diol with Vilsmeyer's reagent in the ratio of phosphorus chloride to substrate 1:1 in dimethylformamide [7].

The target bisazomethines, 5,5'-{1,2-ethylenebis [azanilidenemethylidene]} bis (2-methylpyrimidine -4,6-diol) and 5,5'-{propane-1,2-diylbis [azanilidenemethylidene]} bis (2-methylpyrimidine-4,6-diol), were prepared by the interaction of 4,6-dihydroxy -2-methylpyrimidine-5- carbaldehyde with bisnucleophilic components such as ethane-1,2-diamine and propane-1,2-diamine in a ratio of 2:1 in aqueous medium with the addition of catalytic amounts of acetic acid (Fig. 2).

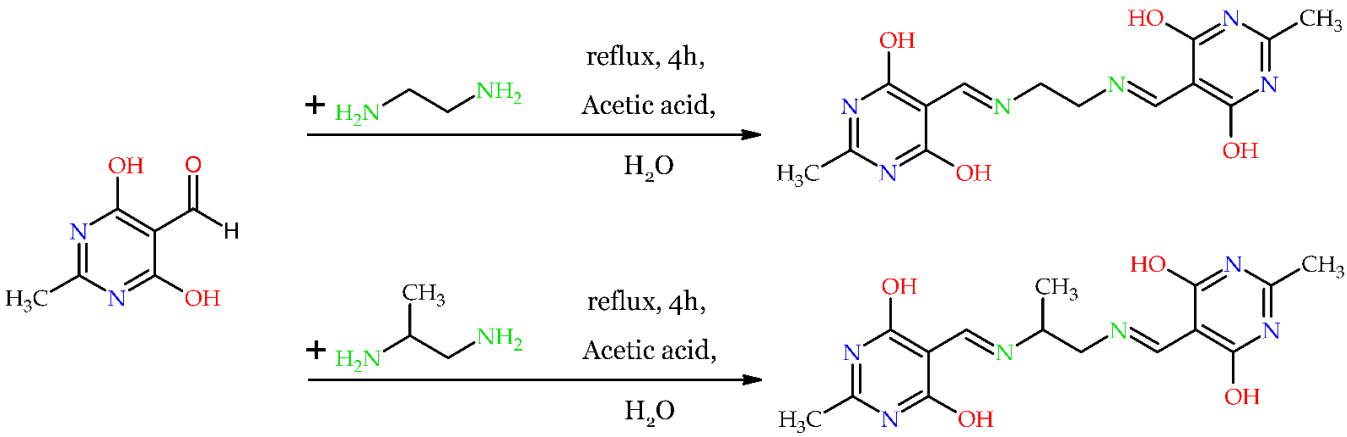

Figure 2: Scheme for the synthesis of bisazomethine derivatives based on 4,6-dihydroxy-2-methylpyrimidine-5-carbaldehyde

The synthesis was monitored by thin-layer chromatography by the absence of substrate 1 in the reaction mass. A mixture consisting of methanol, dichloromethane and hexane in the ratio of 1:9:1 was used as a mobile phase. Detection was performed at 254 nm (UV). The structure of the products was proved by ^{1}H and ^{13}C nuclear magnetic resonance spectroscopy.

2.1. Synthesis of 5,5'-{ethane-1,2-diylbis [[azanilidenemethylylidene]] bis(2-methylpyrimidine-4,6- diol) (2)

4,6-dihydroxy-2-methylpyrimidine-5-carbaldehyde was suspended in 20 mL of water in an amount of 0.22 grams (1.42 mmol) and to this suspension was added 0.04 grams (0.7 mmol) of ethane-1,2-diamine and a catalytic amount of acetic acid (0.03 mmol). The reaction mixture was further heated with a reflux condenser for 4 hours under constant stirring. The synthesis was monitored by thin layer chromatography by the absence of substrate **1** in the reaction mixture. The obtained beige precipitate was filtered off. The practical yield of product **2** was 85%.

Nuclear magnetic resonance spectrum data ^{1}H (400 MHz, DMSO-d_6), δ, ppm, of product **2**: 2.23 s (5.99H, -CH_3), 3.62 s (3.78 H, -CH_2-), 8,49 s (1.98 H, N=CH-), 11,44 s (3.64 H, -OH).

Nuclear magnetic resonance spectrum data ^{13}C (100 MHz, DMSO-d_6), δ, ppm, of product **2**: 19.39 (-CH_3), 59.64 (-CH_2-), 98.77 (C_5), 160.12 (C_2), 163.57 (C_4,C_6), 166.87 (N=CH-).

2.2. Synthesis of 5,5'-{propane-1,2-diylbis[azanilidenemethylidene]}bis(2-methylpyrimidine-4,6-diol) (3)

0.22 grams (1.42 mmol) of 4,6-dihydroxy-2-methylpyrimidine-5-carbaldehyde was suspended in 20 mL of water, 0.05 grams (0.7 mmol) of propane-1,2-diamine and a catalytic amount of acetic acid (0.03 mmol) were added to this suspension. The reaction mixture was further heated with a reflux condenser for 4 hours under constant stirring. The synthesis was monitored by thin layer chromatography by the absence of substrate **1** in the reaction mixture. The obtained beige precipitate was filtered off. The practical yield of product **3** was 90% (Fig. 3).

Nuclear magnetic resonance spectrum data ^{1}H (400 MHz, DMSO-d_6), δ, ppm, of product **3**: 1.26 d (3.02H, C_{11}), 2.11 s (5.95 H, C_7, $C_{7'}$), 3.76 m (1.96 H, C_{10}), 4.08 s (1.07 H, C_9), 8.29 s (2H, C_8, $C_{8'}$), 11.38 (3.25H, -OH).

Nuclear magnetic resonance spectrum data ^{13}C (100 MHz, DMSO-d_6), δ, ppm, of product **3**: 18.39 (C_7,$C_{7'}$), 20.19 (C_{11}), 47.64 (C_{10}), 53.74 (C_9), 98.07 (C_5), 160.12 (C_2,$C_{2'}$), 162.77 (C_4,C_6,$C_{4'}$,$C_{6'}$), 167.47 (C_8,$C_{8'}$).

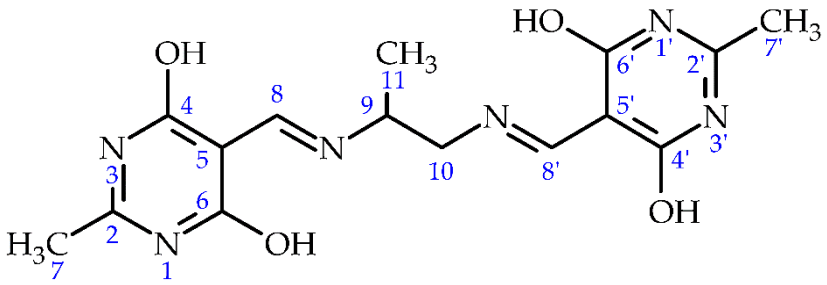

Fig. 3: Structural formula of 5,5'-{propane-1,2-diylbis [azanilidenemethylidene]} bis (2-methylpyri midine-4,6-diol)

III. RESULTS

Based on screening data using the web resources PASS Online, CLC-pred, and Antivir-pred, the obtained compounds exhibit a high probability of antihypertensive activity, oligodendroglioma-targeted activity, and antiviral activity against Dengue virus serotype 2 (Table 1).

Table 1: Results of in silico biological activity screening.

Web resource	Activity	*predicted probability*, Pa
PASS online	I1-imidazoline receptor agonist (antihypertensive)	0.8
CLC-pred	Activity against oligodendroglioma	0.5
Antivir-pred	Antiviral activity against Dengue virus serotype 2	0.3

According to the predicted values of acute toxicity using the web resource GUSAR online, the studied structures belong to class 4 toxicity for intravenous, oral and subcutaneous administration, to class 5 toxicity for intraperitoneal administration (Table 2).

Table 2: Predicted LD50 values depending on route of administration in mg/kg with preliminary assignment to OECD* toxicity classes.

Intraperitoneal	Intravenous	Oral	Subcutaneous
504	158	1785	822
Class 5	Class 4	Class 4	Class 4

**The organisation for economic co-operation and development*

From the above data, it is evident that the compounds potentially have a high safety profile.

The target compounds were obtained by condensation reaction between pyrimidine-5-carbaldehyde and aliphatic diamines. Their structure was reliably proved by ^{1}H and ^{13}C NMR spectroscopy.

Figure 4 shows the 1H NMR (DMSO-d6) spectrum of product 3. The spectrum is characterised by the presence of a singlet signal of the protons of azomethine groups in the region of 8.29 ppm with an integrated intensity of 2.00, a signal of methyl groups bound to pyrimidine rings in the region of 2.11 ppm with an integrated intensity of 5.95 and a hydrogen atom at the tertiary carbon atom in the bridging fragment in the region of 4.08 ppm with an integrated intensity of 1.07. There is also a characteristic multiplet signal of hydrogen atoms of the methylene group of the propylene bridge fragment in the region of 3.76 ppm with an integrated intensity of 1.96, a doublet signal of the methyl group of the bridge fragment in the region of 1.28 ppm with an integrated intensity of 3.02 and a signal of acidic protons of hydroxyl groups in the region of 11.28 ppm.

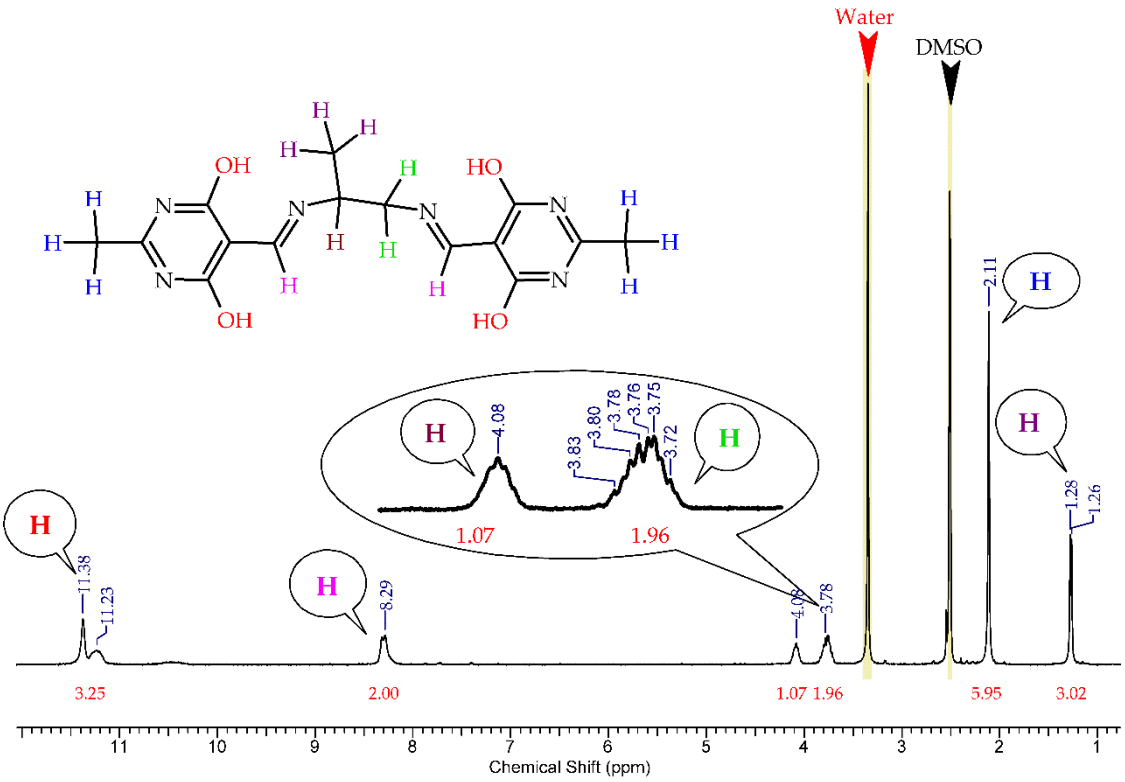

Puc. 4: ^{1}H NMR spectrum of 5,5'-{propane-1,2-diylbis [azanilidenemethylidene]} bis (2-methylpyrimidine-4,6-diol)

IV. CONCLUSIONS

The synthesised compounds are class 4 and 5 according to preliminary acute toxicity screening data. Antihypertensive activity against oligodendroglioma and antiviral activity against Dengue virus serotype 2 are predicted for new bisazomethines with high probability of effect.

The reaction between 4,6-dihydroxy-2-methylpyrimidine-5-carbaldehyde and aliphatic diamines in a 2:1 molar ratio yields novel bisazomethine compounds with isolated yields of 85% and 90%. These derivatives show dual promise as both pharmacologically active agents per se and as synthons for novel metal-organic complexes, which likewise exhibit potential broad-spectrum bioactivity.

REFERENCE

1. Vitaku, E.; Smith, D. T.; Njardarson, J. T. Analysis of the Structural Diversity, Substitution Patterns, and Frequency of Nitrogen Heterocycles among U.S. FDA Approved Pharmaceuticals. J. Med. Chem. 2014, *57* (24), 10257–10274. DOI: 10.1021/jm501100b.
2. Neumann D. M. et al. Synthesis and antifungal activity of substituted 2, 4, 6-pyrimidinetrione carbaldehyde hydrazones //Bioorganic & medicinal chemistry. – 2014. – Vol. 22. – №. 2. – P. 813-826. DOI: 10.1016/j.bmc.2013.12.010
3. Chiriapkin, A. S., Kodonidi, I. P., Pozdnyakov, D. I., & Zolotych, D. S. (2021). Synthesis and QSAR of new azomethine derivatives as agents for the treatment of Alzheimer's disease. Pharmacologonline, *3*, 563-584.
4. Zayed, E. M., Hindy, A. M., & Mohamed, G. G. (2019). Coordination behaviour, molecular docking, density functional theory calculations and biological activity studies of some transition metal

complexes of bis-Schiff base ligand. Applied Organometallic Chemistry, 33(1), DOI: 10.1002/aoc.4525
5. Chioma, F., Okpareke, O., Okafor, S. N., & Ezugwu, C. I. (2023). Antimicrobial, antioxidant, and in silco studies of divalent metal complexes of novel aminopyrimidine Schiff base chelators. Journal of Molecular Structure, 1291, 136070. DOI:10.1016/j.molstruc.2023.136070
6. PASS Online. Prediction of Activity Spectra for Substances. Version 2.0; Institute of Biomedical Chemistry: Moscow, Russia. URL: http://www.way2drug.com/passonline/
7. Dambaev, A. V., Kolesnik, D. A., Yakovlev, I. P., & Semakova, T. L. (2024). Formylation of 2-Methylpyrimidine-4,6-diol Under the Conditions of the Vilsmeier–Haack Reaction. Chemistry Proceedings, 16(1), DOI: 10.3390/ecsoc-28-20128

Unveiling the Interplay of Thickness, Band Gap and Temperature in CIGS Solar Cells

Albert Sebastian, Keerthana M Sajith, Megna Das, & Sijo A K

ABSTRACT

This work reports one-dimensional simulation-based analysis of the performance of thin-film solar cells using Copper Indium Gallium Selenide (CIGS) as the absorber layer. The study focuses on how three key parameters; absorber layer thickness, band gap energy and operating temperature influence the efficiency of solar cells. Simulations were performed using SCAPS-1D under standard illumination conditions (AM1.5G, 1000 W/m²). The absorber layer thickness was varied from 0.8 µm to 2.0 µm, the band gap from 0.8 eV to 1.8 eV and the temperature from 240 K to 360 K. Results show that an optimal combination of these parameters; CIGS thickness of 1.6 µm, band gap of 1.4 eV and operating temperature of 240 K yields a maximum conversion efficiency of 19.95 %. The trends indicate that increasing thickness and band gap improve efficiency up to a limit, beyond which recombination or reduced light absorption lowers performance. Similarly, higher temperatures result in efficiency loss due to increased carrier recombination. These findings provide insight into absorber layer design and optimization for improving the performance of thin-film CIGS solar cell

Keywords: CIGS, SCAPS 1D, solar cells, bandgap, absorber layer thickness, simulation.

Classification: LCC Code: TK2960,,

Language: English

Great Britain Journals Press

LJP Copyright ID: 925684
Print ISSN: 2631-8490
Online ISSN: 2631-8504

London Journal of Research in Science: Natural & Formal

Volume 25 | Issue 8 | Compilation 1.0

Unveiling the Interplay of Thickness, Band Gap and Temperature in CIGS Solar Cells

Albert Sebastian[α], Keerthana M Sajith[σ], Megna Das[ρ] & Sijo A K[ω]

ABSTRACT

This work reports one-dimensional simulation-based analysis of the performance of thin-film solar cells using Copper Indium Gallium Selenide (CIGS) as the absorber layer. The study focuses on how three key parameters; absorber layer thickness, band gap energy and operating temperature influence the efficiency of solar cells. Simulations were performed using SCAPS-1D under standard illumination conditions (AM1.5G, 1000 W/m²). The absorber layer thickness was varied from 0.8 µm to 2.0 µm, the band gap from 0.8 eV to 1.8 eV and the temperature from 240 K to 360 K. Results show that an optimal combination of these parameters; CIGS thickness of 1.6 µm, band gap of 1.4 eV and operating temperature of 240 K yields a maximum conversion efficiency of 19.95 %. The trends indicate that increasing thickness and band gap improve efficiency up to a limit, beyond which recombination or reduced light absorption lowers performance. Similarly, higher temperatures result in efficiency loss due to increased carrier recombination. These findings provide insight into absorber layer design and optimization for improving the performance of thin-film CIGS solar cells.

Keywords: CIGS, SCAPS 1D, solar cells, bandgap, absorber layer thickness, simulation.

I. INTRODUCTION

The pursuit of sustainable energy solutions has sparked significant advancements in solar cell technology, with a growing emphasis on enhancing efficiency and performance. As the world continues to grapple with the challenges of climate change and energy sustainability, the development of more efficient solar cells has become a pressing priority[1]. Solar cells, which convert sunlight into electrical energy, are influenced by a complex interplay of critical parameters, including material thickness, operating temperature, and band gap energy. These factors play a crucial role in determining the overall efficiency and functionality of solar cells, making their analysis and optimization vital for the development of next-generation photovoltaic devices[2].

This study utilizes a one-dimensional simulation tool, SCAPS-1D, to analyze the impact of key parameters on solar cell performance[3]. By leveraging the capabilities of this simulation software, we can gain valuable insights into the behavior of solar cells under various operating conditions[4]. The research focuses on modeling and simulating the behavior of solar cells under varying conditions, specifically examining the effects of thickness on photon absorption and charge carrier generation. This involves investigating how different thicknesses of the active layer influence the solar cell's ability to absorb photons and generate charge carriers, which is essential for optimizing device performance[5].

In addition to thickness, temperature variations also play a significant role in determining solar cell efficiency. Changes in temperature can affect the material properties and overall performance of the solar cell, leading to variations in efficiency and output[6]. By simulating the effects of temperature on solar cell performance, one can gain a deeper understanding of the complex relationships between

London Journal of Research in Science: Natural & Formal

temperature, material properties, and device efficiency. This knowledge can be used to develop more efficient solar cells that can operate effectively across a range of temperatures [7].

Furthermore, the band gap energy of the solar cell material also has a profound impact on its spectral response to different wavelengths of light. By exploring the relationship between band gap energy and spectral response, we can identify optimal configurations that enhance solar cell performance and efficiency. This involves analyzing how different band gap energies influence the solar cell's ability to absorb and convert different wavelengths of light, which is crucial for optimizing device performance[8].

By investigating these parameters and their interplay, this study aims to identify optimal configurations that enhance solar cell performance and efficiency. The findings are expected to contribute to the understanding of solar cell dynamics and provide valuable insights for designing and fabricating more efficient photovoltaic devices. Ultimately, this research has the potential to inform the development of next-generation solar cells that are more efficient, sustainable and cost-effective.

II. THEORETICAL BACKGROUND

The performance of a solar cell depends on several material and environmental parameters. In thin-film CIGS solar cells, absorber layer thickness, band gap energy, and operating temperature are particularly critical. Understanding the influence of these parameters is essential for optimizing device efficiency and stability.

2.1 Absorber Layer Thickness

The thickness of the absorber layer plays a dual role in solar cell performance. A thicker layer increases the absorption of incident photons, particularly in the longer wavelength range, thereby generating more electron-hole pairs. However, excessive thickness can also lead to increased recombination losses, as charge carriers may not efficiently reach the contacts. Conversely, a very thin layer may suffer from inadequate light absorption. Thus, a balanced thickness is essential for maximizing both light absorption and carrier collection efficiency[9].

2.2 Temperature

Temperature significantly affects the electrical behavior of solar cells. Higher temperatures generally lead to a reduction in open-circuit voltage (Voc) due to band gap narrowing and increased carrier recombination. This results in a decline in overall efficiency. On the other hand, lower temperatures reduce recombination losses, leading to improved Voc and fill factor (FF). However, they may also reduce carrier mobility slightly. Therefore, thermal management is a crucial aspect of solar cell design and installation. A comprehensive understanding of these parameters provides the foundation for simulation-driven optimization using tools like SCAPS-1D [2].

2.3 Bandgap

The bandgap (eV) determines the range of the solar spectrum that can be effectively absorbed. A wider band gap restricts absorption to higher-energy photons (e.g., blue light), while a narrower band gap allows absorption across a broader range but with lower voltage output. The ideal band gap for single-junction solar cells lies between 1.1 and 1.4 eV, enabling a good compromise between current and voltage output. CIGS offers tunable band gaps within this range, making it a versatile material for optimization [10].

III. METHODOLOGY

This study employs SCAPS-1D (Solar Cell Capacitance Simulator) to simulate a thin-film solar cell structure based on CIGS as the absorber layer. The cell design includes multiple functional layers and contacts, each defined with specific material and electrical parameters. The simulation focuses on analyzing the impact of varying absorber layer thickness, band gap energy, and temperature on solar cell performance.

3.1 Device Structure

The simulated solar cell architecture comprises a multilayer structure, configured from back to front as follows: a molybdenum (Mo) back contact, a copper indium gallium selenide (CIGS) absorber layer, an oxide void CIGS (OVC) passivation layer, a cadmium sulfide (CdS) buffer layer, an intrinsic zinc oxide (i-ZnO) window layer and an aluminum-doped zinc oxide (AZO) front contact. Each layer's properties, including thickness, doping, band gap and mobility, were carefully parameterized based on realistic material values to ensure an accurate representation of the solar cell's performance.

3.2 Simulation Parameters

The SCAPS-1D simulation was performed under standard conditions to ensure accurate and reliable results. The illumination was set to the AM1.5G spectrum at an intensity of 1000 W/m², mimicking typical solar radiation[11]. The initial temperature was set to 300 K, and later varied to 240 K and 360 K to investigate the impact of temperature on solar cell performance. The voltage range was set from 0 to 1.0 V to capture the current-voltage characteristics of the solar cell. A total of 100 data points were collected to ensure a detailed and accurate representation of the solar cell's behavior.

The simulator solves fundamental equations, including Poisson's equation and carrier transport equations (continuity and drift-diffusion), to evaluate key performance metrics. These metrics include current-voltage (J-V) and quantum efficiency (QE) curves, providing a comprehensive understanding of the solar cell's behavior and performance[12].

3.3 Layer Configuration and Material Properties

Each layer properties were defined in SCAPS using parameters such as:

Table 1: Material parameters of each layer in the CIGS solar cell

Layer	CIGS	OVC	CdS	i-ZnO
Thickness (μm)	1.2	0.015	0.05	0.08
Bandgap (eV)	1.3	2.7	2.45	3.4
Electron Affinity (eV)	4.5	4.2	4.45	4.55
Doping Type	p-type	n-type	n-type	n-type
Doping Density (cm^{-3})	$1.5x10^{17}$	$1x10^{18}$	$1x10^{15}$	$5x10^{18}$
Electron Mobility (cm^2/Vs)	1000	150	200	50
Hole Mobility (cm^2/Vs)	500	30	10	20

Additional parameters such as carrier mobility, thermal velocities and defect densities were also configured based on literature and standard SCAPS data models.

3.4 Contact Properties

The left and right contacts of the solar cell were defined with specific properties to accurately simulate carrier extraction and interfacial behavior. The left contact, made of Molybdenum (Mo), had a work function of 5.54 eV, while the right contact, composed of Aluminum-doped Zinc Oxide (Al:ZnO), had a work function of 4.54 eV. The surface recombination velocities for both contacts were set to 1.0×10^7 cm/s, representing the rate at which charge carriers recombine at the contact interfaces. Contact tunneling was disabled in the simulation. These settings allowed for a realistic representation of the solar cell's behavior[13].

The simulated solar cell structure, depicted in Figure 1, consists of multiple layers: a Mo back contact, a CIGS absorber layer, an OVC passivation layer, a CdS buffer layer, an i-ZnO window layer, and an Al-doped ZnO front contact. During operation, light enters the solar cell through the top (AZO side), generating charge carriers that are collected through the front and back contacts. This structure and the defined contact properties enable the simulation to accurately model the behavior of the CIGS-based thin-film solar cell[14].

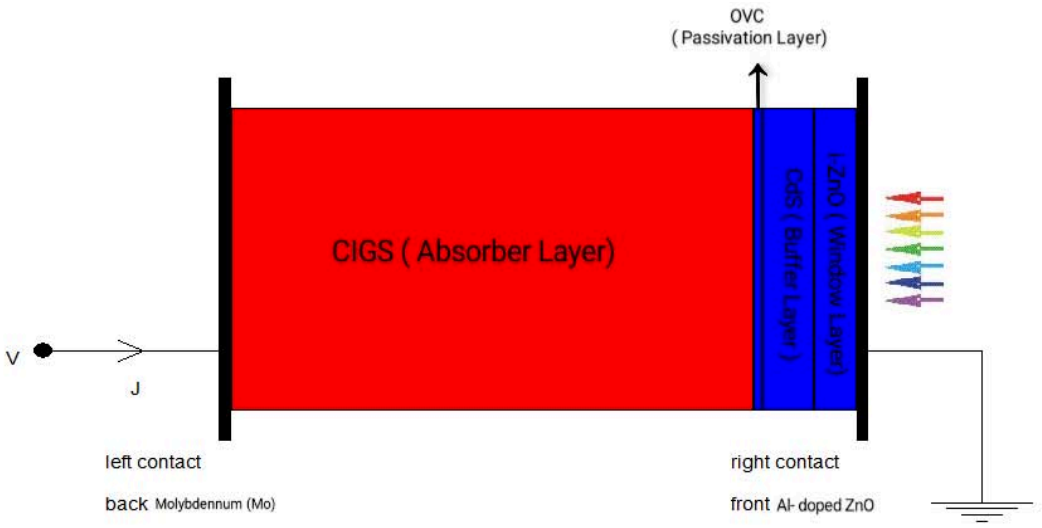

Figure 1: Schematic of the CIGS-based thin-film solar cell simulated in SCAPS-1D

IV. RESULT AND DISCUSSION

4.1 Effect of Absorber Layer Thickness on Solar Cell Efficiency

To evaluate the influence of the absorber layer thickness on device performance, the CIGS thickness was varied while keeping all other parameters constant. The band gap was fixed at 1.2 eV and the simulation was carried out under standard test conditions (AM1.5G illumination, 1000 W/m², 300 K). The thickness of the CIGS layer was varied from [0.800] µm to [2.00] µm in steps of [0.2] µm[15]. The result shown in the figure 2, As the thickness increases: Jsc (Short-Circuit Current Density) rises due to an increase in the optical path length, allowing more photons to be absorbed across the solar spectrum. Thicker layers generate more electron–hole pairs, increasing the photocurrent. This trend continues until most usable photons are already absorbed and further thickness yields diminishing returns[16]. Voc (Open-Circuit Voltage) exhibits minimal variation. Voc is logarithmically related to the ratio of photocurrent to reverse saturation current. While photocurrent increases with thickness,

the reverse saturation current also increases due to enhanced bulk recombination in thicker layers, stabilizing Voc.

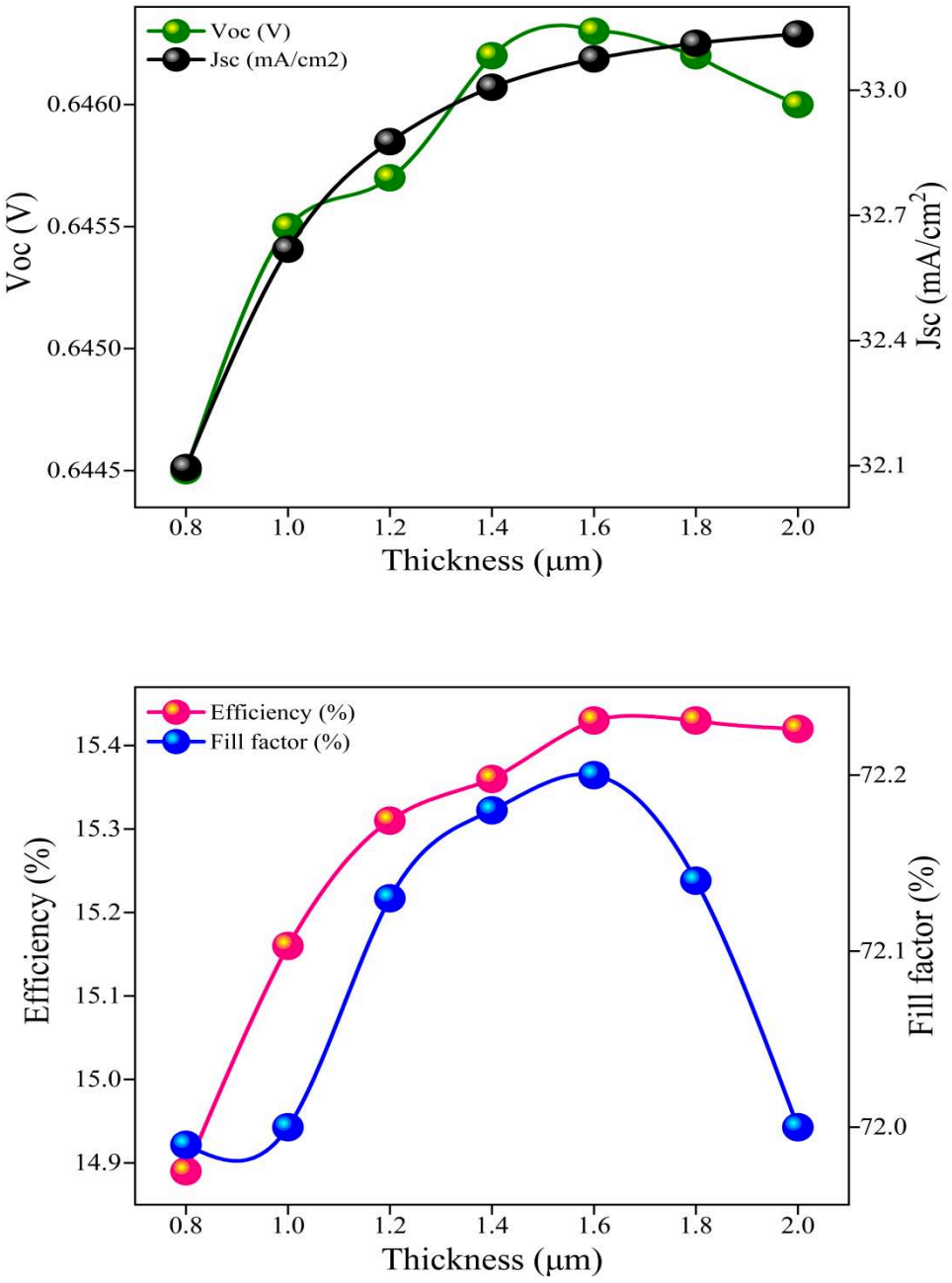

Figure 2: Simulated variation of Jsc, Voc, efficiency and FF with CIGS thickness

FF (Fill Factor) improves initially due to reduced series resistance and better carrier transport in moderately thick layers. However, with further increase, the longer diffusion lengths required for charge carriers to reach the junction result in higher recombination, limiting FF improvement. Efficiency increases and reaches a peaks at 15.43% for a 1.6 μm absorber thickness. Beyond this optimal thickness, recombination losses in the bulk outweigh the benefits of increased photocurrent generation, leading to a slight decline or saturation in efficiency[17].

4.2 Effect of absorber bandgap on solar cell performance

To analyze the influence of the absorber material's band gap on device performance, the band gap of the CIGS layer was varied from 0.8 eV to 1.8 eV, in steps of 0.2 eV, while keeping the thickness fixed at 1 μm. The simulation was conducted under standard conditions (AM1.5G spectrum, 1000 W/m², 300 K)[18].

As shown in Figure 3, the power conversion efficiency increased with the band gap from 0.8 eV to around 1.3–1.4 eV, after which it declined. As the band gap increases, the Voc increases as well. This is because Voc is directly related to the difference between the quasi-Fermi levels of electrons and holes, which becomes larger in materials with wider band gaps. Additionally, a higher band gap reduces the intrinsic carrier concentration, thereby lowering the reverse saturation current and contributing to a higher Voc[19]. The fill factor (FF) also improves with increasing band gap, particularly up to the optimal range of 1.3–1.4 eV. This is primarily due to reduced recombination and more favorable diode characteristics. As the Voc increases and series resistance effects become less dominant, the FF benefits from improved charge extraction efficiency and lower losses in the J-V curve slope near the maximum power point.

However, Jsc decreases with increasing band gap. Although higher band gaps result in better voltage performance, they limit the absorption of lower-energy (longer-wavelength) photons. As a result, fewer photogenerated carriers are created, reducing the current output. This trade-off between increasing Voc and decreasing Jsc is a well-established characteristic in single-junction photovoltaic devices. The overall efficiency follows a non-linear trend, increasing with band gap until a peak is reached (around 1.3-1.4 eV), where the combined effect of optimal Voc, sufficient Jsc, and high FF yields maximum power output. Beyond this point, the loss in Jsc due to reduced spectral absorption outweighs the gains in Voc and FF, leading to a decline in efficiency[20].

The simulation results indicate that an optimal band gap lies between 1.2 eV and 1.4 eV, where the trade-off between voltage and current is balanced, leading to maximum efficiency. This observation agrees with reported values in the literature for CIGS solar cells, where a band gap near 1.3 eV is often cited as ideal for single-junction devices[21].

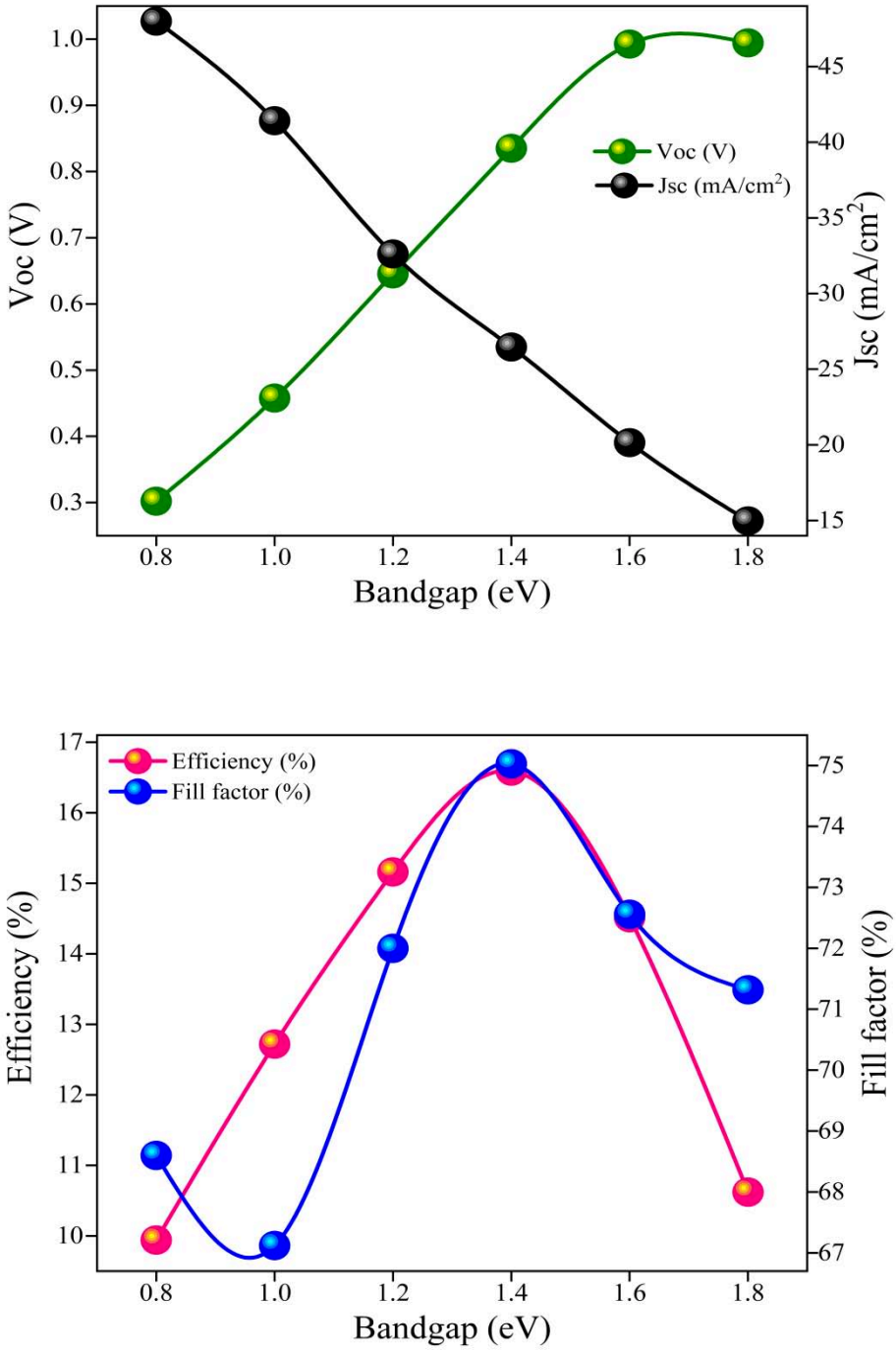

Figure 3: Simulated variation of Jsc, Voc, efficiency and FF with bandgap

4.3 Effect of Operating Temperature on Solar Cell Efficiency

To assess the impact of temperature on solar cell performance, simulations were carried out over a temperature range from 240 K to 360 K in steps of 20 K, while keeping the CIGS absorber thickness fixed at 1 μm and the band gap at 1.2 eV. The results, presented in Figure 4, show a clear decrease in efficiency with increasing temperature[22].

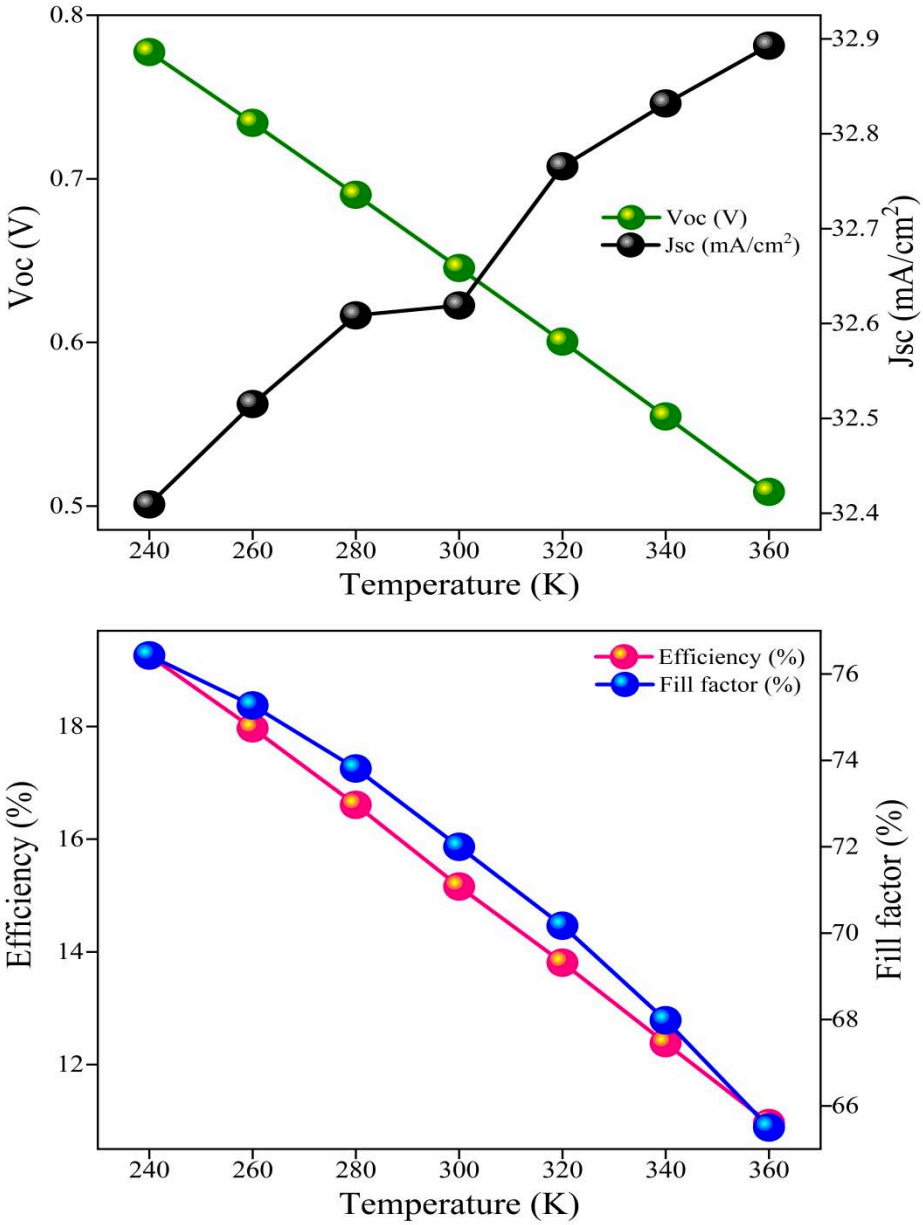

Figure 4: Simulated variation of Jsc, Voc, efficiency and FF with temperature

At lower temperatures (240 K), the device achieved its highest efficiency. As the temperature increases, the open-circuit voltage (Voc) shows a noticeable decrease. This is due to the temperature-induced narrowing of the semiconductor band gap and the exponential increase in reverse saturation current, which lowers the built-in potential. The relationship is governed by the diode equation, where higher thermal energy leads to increased carrier excitation, enhancing recombination and reducing the maximum voltage the device can sustain under open-circuit conditions[23].

Similarly, the fill factor (FF) decreases with rising temperature. Elevated temperatures increase carrier recombination and series resistance effects, while also degrading the ideality of the diode characteristics. As a result, the shape of the current-voltage (J–V) curve becomes less optimal, lowering the FF. On the other hand, the short-circuit current density (Jsc) exhibits a slight increase with temperature. This is because higher thermal energy can enhance carrier generation and mobility to a limited extent[24]. However, this gain is modest and insufficient to overcome the larger losses in Voc and FF. The efficiency drops accordingly, as it is a combined outcome of Voc, Jsc, and FF. The

loss in Voc and FF more than compensates for any minor gain in Jsc, resulting in a net decline in power conversion efficiency at higher temperatures. These trends confirm that thermal effects are detrimental to solar cell performance, primarily due to increased recombination and degraded voltage behavior. Therefore, proper thermal management and material engineering are crucial for maintaining the efficiency of CIGS-based devices, especially in hot environments or under high-intensity illumination.

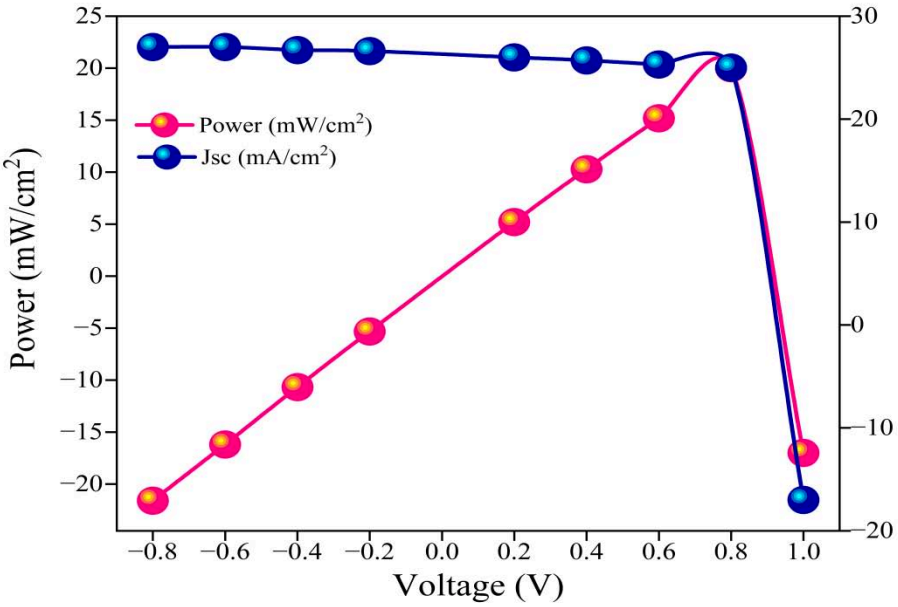

Figure 5: I-V curve of the champion device

4.4 Quantum Efficiency Analysis of Optimized Structure

After evaluating the effects of absorber layer thickness, band gap, and temperature, the solar cell was simulated using optimized parameters: CIGS thickness = 1.6 µm, band gap = 1.4 eV, and temperature = 240 K. The resulting quantum efficiency (QE) curve is shown in Figure 6.

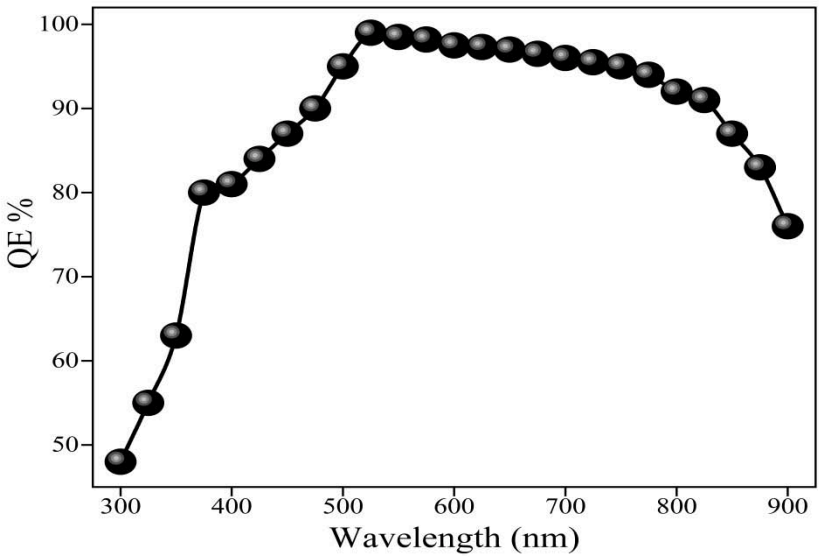

Figure 6: Stimulated quantum efficiency (QE) curve of the optimized solar cell (CIGS thickness = 1.6 µm , band gap = 1.4 eV, temperature =240 K)

The QE represents the fraction of incident photons converted into charge carriers at each wavelength. The curve exhibits a broad and high quantum efficiency, peaking above 90% in the wavelength range of approximately 350 nm to 900 nm, indicating excellent photon absorption and carrier collection in this range. At shorter wavelengths (below 400 nm), a slight drop in QE is observed due to surface recombination and absorption in the window/buffer layers. At longer wavelengths (>800 nm), the decline in QE is attributed to the limited absorption depth in the absorber layer for low-energy photons[25]. Overall, the QE spectrum confirms that the optimized CIGS solar cell structure exhibits high collection efficiency over a broad portion of the solar spectrum, validating the effectiveness of the chosen material and structural parameters.

IV. CONCLUSION

This study examined how variations in the CIGS absorber layer—specifically its thickness, band gap energy, and operating temperature—affect the efficiency of thin-film solar cells. Through a systematic simulation-based approach, it was found that each parameter plays a critical role in determining the device's overall performance.

The results showed that increasing the absorber layer thickness enhances light absorption and current generation up to an optimal value of 1.6 μm, beyond which efficiency saturates or slightly declines due to increased recombination losses. Band gap tuning revealed that an energy gap of 1.4 eV strikes the best balance between voltage and current output, resulting IN improved efficiency. Temperature analysis showed a clear inverse relationship between operating temperature and efficiency, with the highest efficiency of 19.95% recorded at 240 K, confirming the negative impact of thermal recombination on photovoltaic performance.

Overall, the findings highlight that careful optimization of absorber layer properties is essential for achieving high-performance CIGS solar cells. These insights provide valuable guidance for designing cost-effective and efficient photovoltaic devices for real-world applications.

REFERENCE

1. K Ukoba, K O Yoro, Orevaoghene Eterigho-Ikelegbe, C Ibegbulam, Tien-Chien Jen, Adaptation of solar energy in the Global South: Prospects, challenges and opportunities, Heliyon, 10(7), (2024), e28009, https://doi.org/10.1016/j.heliyon.2024.e28009.
2. Shaker, L.M., Al-Amiery, A.A., Hanoon, M.M. et al. Examining the influence of thermal effects on solar cells: a comprehensive review. Sustainable Energy res. 11, 6 (2024). https://doi.org/10.1186/s40807-024-00100-8
3. Sijo A K, Krishnan A, Sapna P and Tom E (2024) Unlocking high-efficiency solar energy: optimizing P3HT/Si hybrid solar cells through numerical simulation Phys. Scr. 99 115950, https://iopscience.iop.org/article/10.1088/1402-4896/ad826c
4. George G. Njema, Joshua K. Kibet, Silas M. Ngari, Nicholas Rono, Numerical optimization of interface engineering parameters for a highly efficient HTL-free perovskite solar cell, Materials Today Communications, 39, (2024), 108957, https://doi.org/10.1016/j.mtcomm.2024.108957.
5. G. G. Njema, B. C. Mosonik, C. C. Ahia, J. K. Kibet, Chem. Eur. J. 2024, 30, e202403192. https://doi.org/10.1002/chem.202403192
6. Olusola Bamisile, Caroline Acen, Dongsheng Cai, Qi Huang, Iain Staffell,The environmental factors affecting solar photovoltaic output, Renewable and Sustainable Energy Reviews, 208, (2025), https://doi.org/10.1016/j.rser.2024.115073.
7. Mohammed Khalis, Fatima Id Ouissaaden, Soufiane El Khaldi, Hamza Kamel, Fahd Elmourabit, Said Dlimi, Studying effect of temperature on the efficiency of solar cells through the

interpolation method, Hybrid Advances, 6, (2024),100231, https://doi.org/10.1016/j.hybadv.2024.100231.
8. Ehsan Raza, Jolly Bhadra, Muhammad Asif, Fakhra Aziz, Noora J. Al-Thani, Zubair Ahmad, A numerical approach to study the effect of bandgap and electron affinity in HTL-free perovskite solar cells and design of two-terminal silicon/perovskite tandem solar cell, Materials Today Communications, 37, (2023), 107383, https://doi.org/10.1016/j.mtcomm.2023.107383.
9. Bipanko Kumar Mondal, Shaikh Khaled Mostaque, Jaker Hossain, Theoretical insights into a high-efficiency Sb2Se3-based dual-heterojunction solar cell, Heliyon, 8(3), (2022), e09120, https://doi.org/10.1016/j.heliyon.2022.e09120.
10. Pedro H.M. Andrade, Christophe Volkringer, Thierry Loiseau, Antonio Tejeda, Matthieu Hureau, Alain Moissette, Band gap analysis in MOF materials: Distinguishing direct and indirect transitions using UV–vis spectroscopy, Applied Materials Today, 37, (2024), 102094, https://doi.org/10.1016/j.apmt.2024.102094.
11. M A. Scarpulla, Brian McCandless, Adam B. Phillips, et al. CdTe-based thin film photovoltaics: Recent advances, current challenges and future prospects, Solar Energy Materials and Solar Cells, 255, (2023), 112289, https://doi.org/10.1016/j.solmat.2023.112289.
12. Abu Kowsar, Sumon Chandra Debnath, Md. Shafayet-Ul-Islam, Mohammad Jobayer Hossain, Mainul Hossain, AFM Kamal Chowdhury, Galib Hashmi, Syed Farid Uddin Farhad, An overview of solar cell simulation tools, Solar Energy Advances, 5, (2025), 100077, https://doi.org/10.1016/j.seja.2024.100077.
13. Fakharuddin, A., Vasilopoulou, M., Soultati, A., Haider, et al.(2021), Robust Inorganic Hole Transport Materials for Organic and Perovskite Solar Cells: Insights into Materials Electronic Properties and Device Performance. Sol. RRL, 5: 2000555. https://doi.org/10.1002/solr.202000555.
14. Moustafa, M., Al Zoubi, T. & Yasin, S. Optoelectronics Simulation of CIGS-Based Solar Cells Using a Cd-Free Nontoxic ZrSxSe2−x as a Novel Buffer Layer. Braz J Phys 52, 141 (2022). https://doi.org/10.1007/s13538-022-01146-z
15. Imani, S., Seyed-Talebi, S.M., Beheshtian, J. et al. Simulation and characterization of CH3NH3SnI3-based perovskite solar cells with different Cu-based hole transporting layers. Appl. Phys. A 129, 143 (2023). https://doi.org/10.1007/s00339-023-06428-0
16. Soley, S. S., Verma, S., Khatri, N., & Pokhriyal, S. (2024). [Title of the article]. Engineering Research Express, 6(3), 032301. https://doi.org/10.1088/2631-8695/ad5c2d
17. Gaia M.N. Javier, Priya Dwivedi, Yoann Buratti, Ivan Perez-Wurfl, Thorsten Trupke, Ziv Hameiri, Improvements and gaps in the empirical expressions for the fill factor of modern industrial solar cells, Solar Energy Materials and Solar Cells, 253, (2023), 112183, https://doi.org/10.1016/j.solmat.2023.112183.
18. Rubén E. Sánchez-García, Rodrigo Salmón-Folgueras, Orlando Castilleja-Escobedo, José Luis López-Salinas, A novel experimental device for solar radiation simulation: Design and evaluation, Results in Engineering, 26, (2025), 105207, https://doi.org/10.1016/j.rineng.2025.105207
19. George G. Njema, Joshua K. Kibet, Silas M. Ngari, A review of interface engineering characteristics for high performance perovskite solar cells, Measurement: Energy, 2, (2024), 100005, https://doi.org/10.1016/j.meaene.2024.100005.
20. S. Akhil, S. Akash, Altaf Pasha, Bhakti Kulkarni, Mohammed Jalalah, Mabkhoot Alsaiari, Farid A. Harraz, R Geetha Balakrishna, Review on perovskite silicon tandem solar cells: Status and prospects 2T, 3T and 4T for real world conditions, Materials & Design, 211, (2021), 110138, https://doi.org/10.1016/j.matdes.2021.110138.
21. Kirstin Alberi, Joseph J. Berry, Jacob J. Cordell, Daniel J. Friedman, et.al, A roadmap for tandem photovoltaics, Joule, 8(3), (2024), 658-692, https://doi.org/10.1016/j.joule.2024.01.017.

22. Nicolae Spalatu, Robert Krautmann, Atanas Katerski, Screening and optimization of processing temperature for Sb2Se$_3$ thin film growth protocol: Interrelation between grain structure, interface intermixing and solar cell performance, Solar Energy Materials and Solar Cells, 225, (2021), 111045, https://doi.org/10.1016/j.solmat.2021.111045
23. Taylor MootJay B. PatelGabriel McAndrewsEli J. Wolf, Temperature Coefficients of Perovskite Photovoltaics for Energy Yield Calculations, ACS Energy Lett. 2021, 6, 5, 2038–2047, https://doi.org/10.1021/acsenergylett.1c00748
24. A. Mortadi, Y. Tabbai, E. El Hafidi, H. Nasrellah, E. Chahid, M. Monkade, R. El Moznine, Investigating temperature effects on perovskite solar cell performance via SCAPS-1D and impedance spectroscopy, Cleaner Engineering and Technology, 24, (2025), 100876, https://doi.org/10.1016/j.clet.2024.100876.
25. Bülent M. Başol and Brian McCandless "Brief review of cadmium telluride-based photovoltaic technologies," Journal of Photonics for Energy 4(1), 040996 (27 June 2014). https://doi.org/10.1117/1.JPE.4.040996